The Relationship Between El Niño/La Niña Oscillations and Recent Anomaly Time Series of OLR Determined by CERES and AIRS

Joel Susskind, NASA Goddard Space Flight Center[1]
Gyula Molnar, Morgan State University/GESTAR[2]
Lena Iredell, Science Applications International Corporation[3]
Norman G. Loeb, NASA Langley Research Center[4]

[1]J. Susskind, NASA GSFC, Code 613, Greenbelt, MD 20771, Joel.Susskind-1@nasa.gov,
[2]G. Molnar, MSU/GESTAR, NASA, Code 613, Greenbelt, MD 20771, Gyula.I.Molnar@nasa.gov,
[3]L. Iredell, SAIC, NASA, Code 613, Greenbelt, MD 20771, Lena.Iredell@nasa.gov,
[4]N. Loeb, NASA LARC, Mail Stop 420, Hampton, VA 23681, Norman.G.Loeb@nasa.gov

Abstract

This paper compares recent spatial anomaly time series of OLR (Outgoing Longwave Radiation) and OLR_{CLR} (Clear Sky OLR) as determined using CERES and AIRS observations over the time period September 2002 through June 2010. We find excellent agreement in OLR anomaly time series of both data sets in almost every detail, down to the 1 x 1° spatial grid point level. This extremely close agreement of OLR anomaly time series derived from observations by two different instruments implies that both sets of results must be highly stable. This agreement also validates to some extent the anomaly time series of the AIRS derived products used in the computation of the AIRS OLR product. The paper then examines anomaly time series of AIRS derived products over the extended time period September 2002 through April 2011. We show that OLR anomalies during this period are closely in phase with those of an El Niño index, and that the recent global and tropical mean decreases in OLR and OLR_{CLR} are a result of a transition from an El Niño condition at the beginning of the data record to La Niña conditions toward the end of the data period. We show that the relationship between global mean, and especially tropical mean, OLR anomalies to the El Niño index can be explained by temporal changes of the distribution of mid-tropospheric water vapor and cloud cover in two spatial regions that are in direct response to El Niño/La Niña activity which occurs outside these spatial regions.

1. Introduction

OLR (Outgoing Longwave Radiation) is a critical component of the Earth's radiation budget and represents the total radiation going to space emitted by the earth-atmosphere system and integrated over all angles. OLR products have been generated

and monitored globally since 1975 based on broad spectral band measurements taken at a given satellite zenith angle by the ERB instrument on the Nimbus-6 and Nimbus-7 satellites (Jacobowitz et al. 1984, Kyle et al. 1993); the ERBE instrument on NOAA-9 and NOAA-10; ERBS (Barkstrom 1989), the AVHRR instrument on NOAA operational satellites (Gruber et al., 1994 and references therein); and most recently by CERES which has flown on EOS Terra since 2000 and EOS Aqua since 2002 (Wielicki et al. 1996).

OLR has been widely used as a proxy for tropical convective activity and rainfall, particularly in diagnosing and understanding tropical intraseasonal to interannual variability and monsoons (e.g., Chiodi and Harrison 2010, Kidson et al. 2002, Hoyos and Webster 2007, Barlow et al. 2005, Kiladis et al. 2005, Jones et al. 2004, Wong et al. 2008, Loeb et al. 2011). In addition, OLR has been used in studies of earth's radiation balance (e.g. Clement and Soden, 2005; Fasullo and Trenberth, 2008) and atmospheric model validation (e.g. Allan et al. 2003). More importantly, anomalies and trends of OLR have been used to study climate feedbacks and processes (e.g. Chung et al. 2010, Huang and Ramaswamy 2009, Soden and Held 2006, Chu and Wang, 1997, Soden et al. 2008, Dessler et al. 2008, Dessler 2010, Trenberth et al. 2010).

OLR at a given location is affected primarily by the earth's skin surface temperature, T_{skin}; skin surface spectral emissivity, ϵ_ν; atmospheric vertical temperature profile, T(p), and water vapor profile q(p); and the heights, amounts, and spectral emissivities of multiple layers of cloud cover. OLR also depends on the vertical distribution of trace gases such as O_3, CH_4, CO_2, and CO. OLR can be computed for a specific Field of Regard (FOR), given all the needed geophysical parameters, using an

OLR Radiative Transfer Algorithm (RTA). Mehta and Susskind developed such an OLR RTA used in conjunction with the TOVS (TIROS Operational Vertical Sounder) retrieval methodology (Susskind et al. 1997) in order to generate the TOVS Pathfinder Path-A OLR data set (Mehta and Susskind 1999a, 1999b). AIRS OLR is computed using AIRS/AMSU sounding products in a completely analogous manner, including use of the same Mehta and Susskind OLR RTA (Susskind et al. 2003).

AIRS measures IR channel radiances over the interval 650 cm^{-1} to 2668 cm^{-1}. Most AIRS results shown in this paper were derived using the AIRS Science Team Version-5 retrieval algorithm (Susskind et al. 2011) which generates values of T_{skin}, ϵ_v, T(p), q(p), O_3(p), cloud parameters, OLR, and OLR_{CLR} valid for each AIRS 45 kmx45 km FOR. The AIRS Version-5 OLR product, referred to as F below, is computed as a sum of 14 spectral components according to

$$F = \sum_{j=1}^{14} F_j = \sum_{j=1}^{14} \left(1 - \alpha\varepsilon_{1j} - \alpha\varepsilon_{2j}\right) F_{j,CLR} + \alpha\varepsilon_{1j} F_{j,CLD1} + \alpha\varepsilon_{2j} F_{j,CLD2} \qquad (1)$$

where $F_{j,CLR}$ is the computed clear sky flux going to space integrated over all angles emanating from spectral band j; $F_{j,CLDk}$ is the analogous flux emanating from an opaque cloud at cloud top pressure p_k; and $\alpha\varepsilon_{kj}$ is the radiatively effective cloud fraction which is the product of the geometric fractional cloud cover α_k for the cloud at pressure p_k as seen from above and the emissivity of that cloud in spectral interval j.

Mehta and Susskind parameterize F_j for a given sounding as a function of the retrieved surface skin temperature, surface spectral emissivity ε_j in spectral band j, and atmospheric temperature, water vapor, and ozone profiles. The parameterization coefficients used by Mehta and Susskind are computed based on line-by-line calculations (Susskind and Searl, 1978) which use the atmospheric line parameter data

base of McClatchey et al. (1972). The spectral intervals used in Equation 1 range from 2 cm^{-1} through 2750 cm^{-1}. There is no need to make radiometric measurements at all frequencies in order to perform the calculation shown in Equation 1.. The surface spectral emissivity ε_v is determined as a function of frequency over the AIRS spectral range using AIRS observations. Surface emissivities at frequencies lower than 650 cm^{-1} are set equal to those at 650 cm^{-1} and are irrelevant with regard to the computation of OLR in any event because the atmosphere is opaque at those frequencies. The AIRS Version-5 retrieval algorithm determines the effective cloud fraction $\alpha\varepsilon_{kj}$ at 800 cm^{-1} for each of two cloud layers k. $\alpha\varepsilon_k$ and is assumed to be independent of frequency in the calculation of OLR. No other approximations are made in the calculation of Equation 1. AIRS OLR_{CLR}, the clear sky OLR, is also a computed product obtained using Equation 1 but setting both $\alpha\varepsilon_1$ and $\alpha\varepsilon_2$ equal to zero. Geophysical parameters are determined from AIRS observations under both cloud-free and cloudy conditions, though their quality is poorer under very cloudy conditions. The CERES OLR_{CLR} product provides OLR for CERES footprints observed to be cloud-free according to coincident MODIS spectral radiance measurements. The MODIS cloud mask used by CERES is described in Minnis et al. (2011).

2. Overview of the Paper

This paper has two main thrusts. The first thrust of the paper is its comparison of values of OLR and OLR_{CLR} determined using CERES and AIRS observations, and their anomaly time series, over the time period September 2002 through June 2010. This comparison shows that the CERES and AIRS OLR anomaly time series are in very close agreement with each other. Agreement of OLR anomaly time series, obtained by

two different instruments in two very different manners, is a very significant finding as it lends credence to the scientific validity of the results obtained from each instrument. A close agreement of OLR anomaly time series derived using two different approaches does not necessarily imply agreement of the OLR_{CLR} anomaly time series, however, because OLR_{CLR} is more difficult to obtain via either approach.

With regard to AIRS, OLR_{CLR} is a computed product using the retrieved geophysical parameters. Retrieved geophysical parameters are generally of poorer accuracy under very cloudy conditions, especially at or near the surface. For this reason, the AIRS Version-5 OLR_{CLR} product is computed only for cases in which the AIRS retrieved cloud fraction is less than 90% and which also pass an OLR_{CLR} quality control procedure which indicates the retrieval is of acceptable accuracy down to the surface (Susskind et al. 2011). We produce successful AIRS Version-5 OLR_{CLR} products in roughly 75% of the scenes observed by AIRS. OLR is always computed from AIRS data, both because of the need for complete sampling, and also because computed values of OLR are not affected significantly by surface and atmospheric conditions beneath the cloud in very cloudy cases. With regard to CERES, spurious values of OLR_{CLR} could occur if a scene which is considered to be clear actually contained some residual cloud cover. The largest factor that would negatively affect the comparison of OLR_{CLR} anomaly time series obtained from AIRS and CERES results from the sampling differences between the two sets of cases included in each ensemble.

Both AIRS and CERES OLR data sets show that a linear fit through their respective global mean monthly mean anomaly time series over the period of

September 2002 through April 2010 contains a substantial negative slope, on the order of -0.075 W/m^2/yr, and an even larger decrease of tropical mean OLR on the order of -0.1 W/m^2/yr. There are very large spatial variations of the changes in OLR in the tropics, with local values ranging from -2.8 W/m^2/yr to +3.1 W/m^2/yr. We observe a correlation of 0.95 between the spatial patterns of changes found in the in AIRS and CERES OLR data sets during this time period. In addition, slopes of the linear least squares fits of monthly mean anomaly time series averaged over different spatial regions agree on the order of ± 0.01 W/m^2/yr and the spatial-temporal correlation of the two sets of the OLR anomaly time series in the tropics is 0.993. This extremely close agreement of OLR anomaly time series derived from observations by two different instruments, and determined in totally independent and different manners, implies that both sets of results must be highly stable. This level of agreement strengthens the overall confidence in the ability of spaceborne sensors to detect large scale global signals and allowing the creation of more reliable multi-sensor, merged data sets. This agreement also validates to some extent the AIRS derived products used in the computation of the AIRS OLR product. Furthermore this agreement indicates we can use the anomaly time series of AIRS derived products to explain the factors contributing to the anomaly time series of both the AIRS and CERES OLR products.

The second thrust of the paper examines anomaly time series of AIRS derived products over the extended time period September 2002 through April 2011. We show OLR anomalies during this period are closely in phase with those of an El Niño index, and the global and tropical mean decreases in OLR and OLR_{CLR} are a result of a transition from an El Niño condition at the beginning of the data record to La Niña

conditions at the end of the data period. The relationship between global mean, and especially tropical mean, OLR anomalies to the El Niño index can be explained by temporal changes in two spatial regions of the distribution of mid-tropospheric water vapor and cloud cover that are in direct response to El Niño/La Niña activity which occurs outside of these regions. One of these regions is east of the area of El Niño/La Niña activity, and the second region is south-southwest of that area. Changes in otherwise global mean and tropical mean OLR, but computed in areas excluding these two regions, are very close to zero over the time period under study.

3. AIRS and CERES OLR data sets used

In this paper we primarily use the operational monthly mean OLR and OLR_{CLR} data products derived using the AIRS and CERES Science Team methodologies respectively. We obtained the AIRS OLR from the Goddard DISC and the CERES products from the Langley ASDC. AIRS was launched on the EOS Aqua satellite in a 1:30 AM/PM local crossing time orbit in May 2002. The operational processing of AIRS data began after AIRS became stable in September 2002. We use the AIRS Version-5 monthly mean Level-3 1° x 1° latitude-longitude grid products which contain separate products generated for each of the 1:30 AM and PM local time orbits. We averaged the AM and PM products together to generate and use a single monthly mean product on the 1° x 1° grid for each month included in the data set. In addition to AIRS OLR and OLR_{CLR}, we also use AIRS Level-3 T_{skin}, q(p), and $\alpha\varepsilon$ cloud products to analyze the factors contributing to the anomaly time series of OLR and OLR_{CLR}.

CERES has flown on both EOS Terra, which was launched in December 1999 on a 10:30 AM/PM local crossing time orbit, as well as EOS Aqua, the same platform that

carries AIRS. The CERES Science Team generates a number of different OLR data sets using CERES observations. The latest versions of the longest record CERES OLR data sets are referred to as the CERES SSF1deg-lite Edition-2.5 data sets, which like AIRS, are presented on 1° x 1° latitude-longitude grid. At the time of this writing, the CERES Terra Edition-2.5 OLR data sets extended to June 2010, the CERES Aqua Edition-2.5 OLR data sets extended to February 2010, and the AIRS Level-3 products extended to April 2011. CERES SSF1deg-lite Edition-2.5 uses the latest calibration improvements (Priestley et al. 2011) with Edition-2 CERES cloud retrievals (Minnis et al. 2008, Minnis et al. 2011), angular dependence models (Loeb et al. 2005), and time-space averaging (Young et al. 1998).

This paper also shows some results comparing OLR computed using the prototype AIRS Version-6 Science Team retrieval algorithm with the Version-5 OLR product computed for the same days. AIRS Version-6 uses an improved OLR RTA (Iacono et al. 2008) in the computation of OLR. This new RTA has two important upgrades compared to Mehta and Susskind (1999a,b). Most significantly, the new OLR RTA is generated using more up to date line absorption parameters, especially for the very strong water vapor absorption band near 300 cm^{-1}. In addition, the new OLR calculation allows for inclusion of the effects of variations in CO_2 concentration over time, as well as those of other minor absorption species such as CO, CH_4, and N_2O, in the calculation of OLR. The Version-5 OLR RTA did not include these effects and parameterized atmospheric transmittances only in terms of variable temperature, water vapor, and ozone. The AIRS Version-6 retrieval algorithm also has other improvements in methodology which lead to improved values of the geophysical parameters

themselves. The AIRS Science Team Version-6 retrieval algorithm is expected to become operational in late 2011. We obtained the OLR results shown in the paper from JPL. They are not available to the public at this time.

4. Comparison of AIRS and CERES OLR and OLR_{CLR} Data Records

Figure 1a shows global monthly mean values of AIRS OLR, as well as CERES Aqua and CERES Terra Edition-2.5 OLR (henceforth referred to as CERES Aqua and CERES Terra OLR) for the period starting September 2002 and extending until the end of each of the current data sets. This figure, as well as subsequent figures, contains no smoothing unless otherwise noted. Figure 1b shows analogous results for OLR_{CLR}. The AIRS OLR time series contains the symbol * on the months November 2003 and January 2010. AIRS OLR and OLR_{CLR} products for parts of these months were missing from the daily AIRS data record. We generated AIRS monthly mean OLR products for these months synthetically, on a grid box basis, by setting grid point differences between AIRS and CERES OLR for an incomplete month equal to the average value of the corresponding AIRS/CERES difference for the previous and subsequent month. We used the same procedure to generate the AIRS OLR_{CLR} data records for those two months. We use these synthetic OLR and OLR_{CLR} monthly mean records as if they were actual observations in the subsequent discussion.

Some monthly mean CERES OLR_{CLR} data points for individual 1° x 1° grid boxes have also been synthesized because either no CERES OLR_{CLR} monthly mean data existed for these grid points or the data values were outliers when compared to AIRS OLR_{CLR} values. For each grid box for each month, we first eliminated any CERES OLR_{CLR} value that differed by more than 20 W/m^2 from the corresponding AIRS OLR_{CLR}

value. Roughly 2% of the CERES OLR_{CLR} monthly mean gridded values were eliminated using this criterion. We then spatially interpolated the remaining values of the difference, CERES OLR_{CLR} minus AIRS OLR_{CLR}, to generate synthetic values for the missing grid boxes. These synthetic differences were then added to the AIRS OLR_{CLR} product for the corresponding grid box to generate the synthetic value of CERES OLR_{CLR} which is used in all subsequent calculations.

We observe a number of features apparent from Figures 1a and 1b. The most prominent result is that to first order, the AIRS and CERES OLR data sets appear to be biased compared to each other, as are the AIRS and CERES OLR_{CLR} data sets. Figures 2a and 2b show the differences between the monthly global mean values of OLR and OLR_{CLR} shown in Figures 1a and 1b, as well as the difference between CERES Terra and CERES Aqua. Figures 2a and 2b also contain dashed lines showing the average value of each difference. AIRS Version-5 OLR shows a nearly constant bias, with an average value of 9.05 W/m^2, compared to CERES Terra and 9.49 W/m^2 compared to CERES Aqua OLR. We observe a small essentially repetitive seasonal cycle, with maxima and minima in June and December respectively, in the difference between AIRS and CERES Terra OLR. Part of this annual cycle in the difference between AIRS and CERES OLR may be the result of the large diurnal cycle of OLR over land. CERES tries to capture the diurnal cycle by fitting the data at the Terra and Aqua overpass times (twice per day at low latitudes) with a half-sine fit (Young et al. 1988). AIRS averages daytime and nighttime OLR observations together but does not make any other correction for diurnal cycle. The difference between AIRS and CERES Aqua OLR is similar to that between AIRS and CERES Terra OLR, but somewhat more variable

over time. CERES Terra OLR is slightly larger than CERES Aqua OLR, especially before January 2005. As with AIRS OLR, there is a small mostly repetitive annual cycle in the difference between CERES Terra OLR and CERES Aqua OLR from 2005 on. The differences between AIRS and CERES OLR_{CLR} are similar to, but smaller than, those of OLR, with regard to their mean value and their seasonal cycle. The mean value of AIRS minus CERES Terra OLR_{CLR} is 6.37 W/m^2, which is roughly 2.7 W/m^2 less than that of AIRS minus CERES Terra OLR.

The large biases between AIRS and CERES OLR and OLR_{CLR} data records are at first disconcerting but are readily understood. The AIRS OLR product derived using the AIRS Science Team Version-6 retrieval algorithm, which will become operational in late 2011, is expected to have much smaller biases compared to CERES Terra OLR than does AIRS Version-5 OLR. The nearly constant bias between OLR as computed based on AIRS products and observed by CERES is primarily a result of the use of an old set of line by line absorption coefficients in the parameterization of the Version-5 OLR RTA (Mehta and Susskind 1999a,b), compared to the improved OLR RTA (Iacono et al. 2008) used in Version-6. The main difference between the two OLR parameterizations is that Iacono et al. (2008) has more absorption in the water vapor rotational band than does Mehta and Susskind (1999a). This change would tend to generate lower values of OLR, especially under very moist conditions.

We tested the latest version of the AIRS Version-6 retrieval algorithm on seven days in different years and different seasons, ranging from September 6, 2002 through May 20, 2010. The difference in OLR between the two versions has significant spatial variability even on a given day. In most cloudy areas, which are less sensitive to

absorption by tropospheric water vapor, Version-6 OLR tends to be higher than Version-5 OLR. Conversely Version-6 OLR tends to be considerably lower than Version-5 OLR in most regions away from clouds, especially for moister cases. Figure 3a shows the spatial distribution of the difference between the 7-day average of OLR computed using Version-6 and computed using Version-5. Figure 3b shows analogous results for OLR_{CLR}. The most important point to notice is that the Version-6 global mean OLR averaged over seven days is lower by 7.06 W/m^2 than the Version-5 global mean OLR product. This indicates that AIRS Version-6 global mean OLR should agree with CERES Edition-2.5 OLR to within about 2 W/m^2. Figure 3b shows that global mean Version-6 OLR_{CLR} for these seven days is 7.54 W/m^2 less than Version-5 OLR_{CLR}. This suggests that AIRS Version-6 OLR_{CLR} will also be very close to CERES OLR_{CLR} on the average.

Table 1a shows values of the slopes of the linear least squares fits of the differences among AIRS, CERES Terra and CERES Aqua OLR, as well as the mean differences and standard deviations of these OLR time series over the period September 2002 through August 2009. Table 1b shows analogous results comparing the OLR_{CLR} time series. The comparison statistics are given for this portion of the total overlap time period because it represents differences over a complete 7-year period. It is important that these slopes be compared over complete years to minimize artifacts due to effects of the annual cycle differences in each data set.

The slope of the differences between AIRS and CERES OLR and OLR_{CLR} records over this 7-year time period is not affected to first order by a constant bias and gives a preliminary indication of the stability of different data sets with regard to each

other over the seven year period under study. The slope for the time series AIRS minus CERES Terra OLR is considerably smaller than that of AIRS minus CERES Aqua OLR. The standard deviation between the AIRS OLR and CERES Terra OLR time series is also considerably smaller than that between AIRS OLR and CERES Aqua OLR, and closer to that between CERES Terra OLR and CERES Aqua OLR. These same relative results also hold when comparing time series of OLR_{CLR}. This does not necessarily imply that the CERES Terra OLR record is better than the CERES Aqua OLR record. Nevertheless, based on the results shown in Tables 1a and 1b, and the fact that the CERES Terra OLR data set extended further in time than the CERES Aqua OLR data set, we chose to use the CERES Terra OLR and OLR_{CLR} products in the OLR comparisons between CERES and AIRS shown in the remainder of this paper.

5. Comparison of AIRS and CERES Terra OLR Anomaly Time Series

In this section, we compare anomaly time series of AIRS and CERES OLR and OLR_{CLR} and their Average Rates of Change (ARC's) computed over different domains: global mean; tropical mean; zonal mean; and grid point by grid point. Anomalies represent differences of monthly mean values of a product from their climatological value as determined by each instrument. Therefore, biases between instrumental records do not affect the relationship between their anomalies to first order. We define the ARC for a given data set as the slope of the linear least squares fit passing through an anomaly time series. We use the term Average Rate of Change to describe the slopes of anomaly time series rather than the term Trend, which is generally used to characterize long-term multi-decadal data sets rather than the seven plus year period studied in this paper. The results show that even though there is a significant bias

between AIRS and CERES data records, there is still an excellent agreement between details of AIRS and CERES OLR and OLR_{CLR} anomaly time series in almost all details.

We generated the monthly mean OLR and OLR_{CLR} climatologies on a 1° x 1° spatial resolution for each month by taking the average of the grid box value for that month over a 7-year time period. OLR and OLR_{CLR} anomalies for a given month in a given year, on a 1° x 1° spatial grid, are defined as the difference between their monthly mean values and their monthly climatologies for that grid box. The area mean anomaly for a given month is the cosine latitude weighted average of the grid box anomalies contained in the area under consideration (Global, Tropical, North America etc.).

5.1. Global Mean and Tropical Mean Anomaly Time Series

This section compares global mean and tropical mean anomaly time series of AIRS and CERES OLR and OLR_{CLR}. Changes in global mean quantities over time are often used as an indication of whether the earth-atmosphere system has been changing as a function of time (e.g., the discussion of "global warming"). Such a discussion can be misleading, both because changes in the earth-atmosphere system over time are not spatially homogeneous, and also because changes of a parameter over a limited time period are in no way indicative of what may occur over later time periods. We also examine tropical mean anomaly time series. The tropics, defined as the band 20°N through 20°S, constitutes 34% of the area of the globe. As such, features found in tropical monthly mean anomalies can contribute significantly to those found in global monthly mean anomalies.

We show that global and tropical mean anomalies of AIRS and CERES OLR are highly correlated in time with each other, as well as with the AIRS El Niño index. The

AIRS El Niño index represents the monthly mean oceanic sea surface temperature (SST) anomaly determined using the AIRS Version-5 T_{skin} product, averaged over the spatial area 15˚N to 15˚S latitude and 140˚W westward to 160˚E longitude. The reason for the selection of this El Niño area will be discussed later in the paper. We also show reasonably good agreement between AIRS and CERES anomaly time series of OLR_{CLR}, both with each other and with the El Niño index. The latter is an important finding because it demonstrates that while changes in cloud cover in response to El Niño/La Niña activity are playing an important role in the recent decreases of global mean, and especially tropical mean OLR, other short-term changes influenced by El Niño have also taken place that affect OLR_{CLR}.

Figure 4a shows the global anomaly time series of AIRS Version-5 OLR and CERES Terra OLR for the periods September 2002 through April 2011 and September 2002 through June 2010, respectively, as well as the difference between the two sets of monthly mean anomalies for the overlap time period. Figure 4b shows analogous results for tropical mean OLR anomalies, and Figures 5a and 5b show analogous global mean and tropical mean anomaly time series for the AIRS and CERES OLR_{CLR} products. Figures 4b and 5b also include the El Niño index, multiplied by 3 in Figure 4b and by 2 in Figure 5b. Tropical mean OLR and OLR_{CLR} anomalies tend to track those of the El Niño index in phase fairly closely. Amplitudes of the largest tropical mean OLR_{CLR} anomalies also match those of the El Niño index multiplied by 3, and those of OLR_{CLR} anomalies match the El Niño index multiplied by 2. This shows that the longest tropical mean OLR anomalies are roughly 50% larger than the largest tropical mean OLR_{CLR} anomalies. Positive values of the El Niño index (2003, 2005, 2007, early 2010)

correspond to El Niño periods, and negative values (2008, late 2010) correspond to La Niña periods.

Table 2a shows the global and tropical mean values of the Average Rate of Change for AIRS OLR and CERES Terra OLR anomalies over the time period September 2002 through June 2010, the standard deviations between the two sets of global and tropical anomaly time series, and the temporal correlations between each global and each tropical anomaly time series. The uncertainties shown in this table and all other tables represent the 99% confidence interval. The agreement of the Average Rates of Change of both global mean and tropical mean anomaly time series found in the AIRS and CERES OLR records is very good, with a difference of about 0.02 $W/m^2/yr$. The standard deviation of the difference between the two global OLR anomaly time series is considerably smaller than that between the two OLR time series because the effects of the small essentially constant annual cycle in the differences between AIRS and CERES Terra OLR have been removed to first order in the generation of the anomaly time series. In addition to considerations relating to the diurnal cycle of OLR, a part of the small annual cycle in the difference between AIRS and CERES OLR can be attributed to some extent to the fact that there is more water vapor in the atmosphere, and hence a larger error in the Version-5 OLR calculations, in the Northern Hemisphere summer than in the Northern Hemisphere winter. The temporal correlations of the two global and tropical OLR anomaly time series are 0.953 and 0.983 respectively. Both show that global mean OLR has decreased on the average on the order of -0.075 $W/m^2/yr$ over the common time period September 2002 through June 2010, and tropical mean OLR has decreased at a rate of roughly

-0.1 W/m^2/yr from the beginning of the time period to the end. The close agreement of global and tropical mean ARC's of AIRS and CERES OLR anomaly time series is more significant than the values themselves.

Figures 4a and 4b show that an onset of negative mean OLR anomalies began in late 2007, with tropical mean values generally considerably larger than global mean anomalies, especially after mid-2007. The decrease in global mean OLR in late 2007 is strongly influenced by the significant reduction in tropical mean OLR which started a few months earlier. Tropical mean OLR anomalies, and to a lesser extent global mean OLR anomalies, became positive starting in late 2009, roughly coincident with the onset of another El Niño event. The AIRS OLR product, which extends to April 2011, shows that very substantial negative global and tropical mean OLR anomalies occurred in the period starting mid-2010, in which a substantial La Niña event occurred which continues through the time period observed by AIRS shown in this paper. As a result of inclusion of these large negative OLR anomalies, the negative Average Rate of Change of global mean AIRS OLR over the extended time period through April 2011 increased to -0.093 W/m^2/yr, compared to -0.088 W/m^2/yr through June 2010, and the negative ARC of the tropical mean AIRS OLR increased to -0.189 W/m^2/yr compared to -0.113 W/m^2/yr.

Figure 4b shows that the anomaly time series of tropical mean OLR closely follows that of the El Niño index. The ARC of the El Niño index, computed over the extended time period through April 2011, is -0.11K/yr, which indicates that on the average, the El Niño region has been cooling over the last 8 years. The global mean and tropical mean OLR anomaly time series indeed correlate very highly with each other as well as with the El Niño index.

Table 2c shows temporal correlations between global mean and tropical mean anomaly time series of OLR and OLR_{CLR} as well as correlations of anomaly time series with the AIRS El Niño index. Correlations using AIRS time series are shown above the diagonal in bold and those using CERES time series are shown beneath the diagonal. The temporal correlation of the CERES global and tropical mean OLR anomaly time series is 0.55, and the corresponding correlation for the AIRS time series is 0.56. This shows that tropical anomalies provide a significant contribution to the global OLR anomaly time series. The CERES and AIRS tropical mean OLR anomaly time series also correlate highly with the El Niño index, with temporal correlations of 0.68 and 0.69, respectively. Both sets of global OLR anomaly time series also show moderate correlations with the El Niño index which are smaller than those found in the tropics. These correlations of global and tropical anomaly time series with the El Niño index imply that the recent short term decreases in global and tropical OLR are the result of changes from El Niño conditions at the beginning of the time series to La Niña conditions at the end.

One might not expect as good agreement between anomaly time series of CERES OLR_{CLR} as with OLR, if for no other reason than there are significant sampling differences between the cases included in each OLR_{CLR} data set. Given this caveat, it is worthwhile to compare both OLR_{CLR} anomaly time series to see the extent that features found in one data set corroborate the same features found in the other. It is also important to see the extent that features in the OLR_{CLR} anomaly time series are consistent with those of OLR. A considerable agreement between OLR and OLR_{CLR}

anomalies indicates that a substantial part of the OLR anomalies can be attributed to something other than clouds.

Table 2b shows that the AIRS and CERES OLR_{CLR} anomaly time series are highly correlated with each other, though the correlation is not as high as between the OLR time series. Part of the decrease in correlation is a result of the reduction in values of each set of OLR_{CLR} anomalies compared to those of OLR. In addition, the standard deviations of the OLR_{CLR} anomaly differences are somewhat larger than those of OLR. Perhaps more significant is the fact that AIRS and CERES global mean and tropical mean OLR_{CLR} anomaly time series are each very highly correlated with those of OLR as shown in Table 2c. Moreover, each tropical OLR_{CLR} anomaly time series has roughly comparable correlations with the El Niño index as does tropical OLR. This indicates that a considerable portion of global and tropical OLR anomalies are influenced by El Niño/La Niña activity and arise from something other than changes in cloud cover.

While AIRS and CERES OLR_{CLR} anomaly time series are highly correlated with each other, Figures 5a and 5b both show a positive drift in time of the OLR_{CLR} anomaly differences. Table 2b shows that the global and tropical mean values of the ARC's of AIRS OLR_{CLR} are very close to zero, while those of CERES OLR_{CLR} are very close to those of CERES OLR. This apparent discrepancy may well be a result of the significant sampling differences found in the two different OLR_{CLR} data sets.

5.2. The Spatial Distribution of ARC's of OLR and OLR_{CLR}

This section compares the spatial distribution of ARC's of AIRS and CERES OLR and OLR_{CLR} with each other. First, we compare zonal mean ARC's, and then compare ARC's on a ˚1latitude by 1˚ longitude basis. These comparisons not only show

excellent agreement of ARC's of AIRS and CERES OLR products on a small spatial scale, but also depict the spatial regions that have been contributing to the short term decreases in global mean and tropical mean values of OLR over the period under study.

Figure 6a shows the zonal mean ARC's of the AIRS and CERES Terra OLR records for the period September 2002 through June 2010, as well as the difference of the two sets of zonal mean ARC's. There is again excellent agreement between the zonal mean structures of ARC's in both OLR data sets, which have a latitudinal correlation of 0.97. It is apparent from Figure 6a that the majority of the decrease in global OLR during the time period under study originates in the tropics south of 8°N. Other areas of negative OLR ARC's occur near 60°S and 60°N latitudes. OLR increased over this time period north of 70°N. AIRS negative zonal mean OLR ARC's are somewhat larger than those of CERES between 5°S and 45°S and AIRS OLR ARC's are more positive (or less negative) than those of CERES poleward of 70°.

Figure 6b shows analogous results for OLR_{CLR}. With regard to AIRS, the structure of zonal mean ARC's of OLR and OLR_{CLR} are generally similar to each other, with a correlation of 0.86. The agreement is especially good poleward of 60° latitude. AIRS zonal mean OLR_{CLR} ARC's in the tropics are significantly smaller than those of OLR. In addition, there is a major qualitative difference between OLR and OLR_{CLR} near 5˚N latitude, which has a very large negative ARC of AIRS OLR and essentially a zero ARC of AIRS OLR_{CLR}. ARC's of CERES zonal mean OLR_{CLR} are very close to those of AIRS OLR_{CLR} poleward of 60˚N and 60˚S latitudes, but are generally on the order of 0.1 $W/m^2/yr$ more negative between 60˚S and 50˚N. The latitudinal correlation of AIRS and CERES ARC's of zonal mean OLR_{CLR} is 0.92, which is slightly lower than that found for

AIRS and CERES OLR. The latitudinal correlation of ARC's of CERES OLR and OLR_{CLR} is 0.85, which is again similar to the correlation of zonal mean ARC's of AIRS OLR and OLR_{CLR}. The fact that zonal mean ARC's of OLR and OLR_{CLR} are highly correlated with each other shows that much of the cause of the zonal mean structure of OLR ARC's is coming from something in addition to changes in cloud cover.

The spatial distributions of global OLR ARC's over the time period September 2002 through June 2010 are shown in Figures 7a and 7b for AIRS and CERES, respectively. Both fields are presented on the 1° latitude by 1° longitude grid on which the data sets are given. The precise values of the ARC's shown in Figures 7a and 7b are not necessarily meaningful, both because of the limited statistical significance of the value for each grid point taken over a seven year ten month time period, and also because as discussed previously, these values are dependent on the time period over which they are calculated. More significant than the values of the ARC's shown in Figure 7 is their very coherent spatial structure and its implication with regard to atmospheric processes.

Figures 7a and 7b demonstrate two very important points. The first is the virtually indistinguishable spatial distributions of the ARC's of AIRS OLR and of CERES OLR. Figure 7c shows this difference, with a spatial correlation of 0.948, and a standard deviation of 0.18 $W/m^2/yr$. The global mean AIRS OLR ARC for this period is 0.023 $W/m^2/yr$ lower (more negative) than that of CERES Terra. This small difference is not monolithic, but occurs primarily near 30°S latitude, especially over Eastern Australia and South Africa, both of which contain large negative OLR ARC's.

The most important point of Figures 7a and 7b is that not only do OLR Average Rates of Change contain a pronounced zonal mean structure, there is considerable longitudinal structure at given latitudes as well. This longitudinal structure is particularly noteworthy in the tropics. As shown in Figure 7, even though zonal mean tropical OLR ARC's are very negative, indicative of increased zonal mean precipitation over the time period September 2002 through June 2010, positive OLR ARC's as large as 3.2 $W/m^2/yr$, indicative of a mean decrease in precipitation, exist in the vicinity of the equatorial dateline. These are more than compensated for, in the zonal mean sense, by negative OLR ARC's at other longitudes, as large as -2.9 $W/m^2/yr$ near the equator over Indonesia in the vicinity of 120°E longitude.

Figures 7a-c, and some subsequent figures, contain rectangles surrounding the area between 8°N to 20°S and 140°W eastward to 10°E, which we will refer to as OLR Region 1, and the area between 15°S to 30°S and 140°E eastward to 160°W, which we will refer to as OLR Region 2. ARC's of OLR within both these areas are very negative over the period September 2002 through June 2010. The decreases in OLR that took place in these two regions during the period under study will be shown later in the paper to be the major cause of the negative values of the global and tropical mean OLR ARC's shown in Table 1. OLR Regions 1 and 2 were selected entirely based on the results shown in Figure 7 and were chosen both so as to be rectangular and also to encompass key features shown in both Figures 7a and 7b. OLR Region 2 is essentially in the "heart" of the area referred to as the South Pacific Convergence Zone, which varies its location according to the phase of the El Nino – Southern Oscillation (ENSO) and of the Interdecadal Pacific Oscillation (Folland et al. 2002; Brown et al. 2011).

Figures 8a-c show the spatial distribution of ARC's of AIRS and CERES OLR_{CLR} over the time period September 2002 through June 2010, as well as their difference. Regions 1 and 2 are also indicated in these figures. The general agreement of the spatial distribution of ARC's of AIRS and CERES OLR_{CLR} is again very good, with a spatial correlation of 0.762. Figure 8c shows that much of the positive bias of AIRS zonal mean ARC's of OLR_{CLR} compared to CERES between 50°N and 60°N latitude occurs over the oceans. At high latitudes, both the patterns and magnitudes of ARC's of OLR and OLR_{CLR} agree well. In the tropics, however, the patterns of ARC's of OLR and OLR_{CLR} agree well, but the magnitudes of ARC's of OLR are considerably larger than those of OLR_{CLR}. This indicates that changes in cloud cover over the time period under study are playing a major role with regard to changes in tropical OLR, but are playing a much smaller role with regard to changes in extra-tropical OLR.

5.3. Longitudinal Distribution of Equatorial Anomaly Time Series: Hovmöller Diagrams

Figures 7 and 8 show that the tropics contain large spatially coherent areas with alternating values of positive and negative ARC's of OLR and OLR_{CLR} over the time period under study. This section compares Hovmöller diagrams of the longitudinal distribution of tropical anomaly time series of CERES and AIRS OLR and OLR_{CLR}. Agreement of AIRS and CERES tropical Hovmöller diagrams is significant because it demonstrates that there is not only agreement in ARC's of OLR and OLR_{CLR}, but in the tropical OLR anomaly time series themselves. These anomaly time series play a very important role in explaining the tropical distribution of the ARC's of OLR and OLR_{CLR} shown in Figures 7 and 8.

Figures 9a and 9b present Hovmöller diagrams, showing time series of monthly mean OLR anomalies (vertical scale), integrated over the latitude range 5°N through 5°S, in each 1° longitude bin (horizontal scale) for the periods for which AIRS and CERES OLR records exist: September 2002 - April 2011 for AIRS and September 2002 – June 2010 for CERES. The difference between these two figures in the overlap time period is shown in Figure 9c. Figures 9a-9c, and all subsequent Hovmöller diagrams, have a small amount of smoothing applied to them. A five point (5 month) smoothing was applied in the vertical and a fifteen point (15 degree) smoothing was applied in the horizontal to minimize the effects of small discontinuities between adjacent rectangular grid points on the figures. Most of the region covered is ocean. There are three relatively small land areas near the equator: South America, Africa, and Indonesia. These land areas each lie between the three sets of narrow vertical lines shown in Figure 9. There are also two other vertical lines at 140˚W longitude and 10˚E longitude, encompassing the longitudinal range contained within Region 1.

The two sets of Hovmöller diagrams are essentially identical, with a correlation coefficient of 0.993 between them. Some of the largest differences between the AIRS and CERES tropical anomaly time series occur in November 2003 and January 2010, the two months for which AIRS data was synthesized. These differences would have been much larger if the AIRS “monthly mean” OLR products stored at the Goddard DISC were used in the calculations, because in both cases the AIRS “monthly mean” products represented averages over less than a month time period while the CERES data represented observations taken over the entire month. Indeed, when the AIRS data contained at the DISC for these two months was used originally in the generation

of Figure 9, those two months showed pronounced signals in the original Figure 9c. This alerted us to check, and correct for, the cause of this problem.

The anomaly time series shown in Figures 9a and 9b depict the phase relationship of OLR anomalies in different longitudes as a function of time. Such figures in turn provide insight into the spatial distribution of tropical ARC's in the vicinity of the equator such as shown in Figures 7 and 8. In the longitudinal band 160˚W westward to 140˚E, equatorial OLR anomalies were very negative in late 2002/early 2003, corresponding to a period of increased precipitation, and were very positive from mid-2007 through early 2009 corresponding to decreased precipitation. This gave rise to the substantial positive OLR ARC shown in Figure 7 over the region 5˚N – 5˚S, 160˚W to 140˚E. Figure 9a shows that AIRS OLR anomalies in this same region are also very positive starting mid-2010. Therefore, OLR ARC's over the extended time period September 2002 – April 2011 would be even more positive in this area than those shown in Figure 7a covering a shorter time period. Figure 7 shows very negative values of OLR ARC's near the equator between 100˚E and 140˚E longitudes. Figure 9 shows that equatorial OLR anomalies between 100˚E and 140˚E are out of phase with those between 140˚E and 160˚W and are of comparable magnitude. Figures 9a and 9b also show that equatorial OLR anomalies 160˚W eastward to 40˚E , within the longitudinal domain of OLR Region 1, tend to be smaller than, and out of phase with, those from 160˚W westward to 140˚E. This gives rise to the negative equatorial OLR ARC's shown in Figure 7 in OLR Region 1.

Figures 10a-c show analogous results for OLR_{CLR}. The scale of Figure 10 is one third that of Figure 9, so as to better highlight the smaller OLR_{CLR} anomalies. Hovmöller

diagrams of AIRS and CERES OLR_{CLR} anomaly are again in excellent agreement, with a correlation of 0.913 between them. The patterns of OLR_{CLR} anomalies are also very similar to those of OLR, albeit with smaller values of the anomalies, which are roughly one-third the value of the OLR anomalies. Hovmöller diagrams of AIRS OLR and OLR_{CLR} have a spatial-temporal correlation of 0.793 with each other over the time period September 2002 – June 2010, and those of CERES OLR and OLR_{CLR} have a correlation of 0.697. This again demonstrates that while temporal changes in cloud cover are playing a very large role in tropical OLR anomalies, other factors which are in phase with changes in cloud cover play a significant role as well.

6. The Effect of Phases of El Niño/La Niña on Tropical Water Vapor, Cloud Cover, and OLR Anomaly Time Series

Figures 4 to 10 show that the spatial patterns of the AIRS and CERES Average Rates of Change of OLR and OLR_{CLR} over the time period September 2002 through June 2010 are in excellent agreement with each other, as are their anomaly time series averaged over different spatial regions. Both CERES and AIRS OLR products show that the common time period under study is marked by a substantial decrease in global OLR, on the order of -0.075 $W/m^2/yr$, averaged over the globe and -0.10 $W/m^2/yr$ averaged over the tropics. This agreement of Average Rates of Change of OLR anomaly time series derived from observations by two different instruments, in totally independent and different manners, implies that both sets of OLR products must be stable over the 7 year 10 month period in which they were compared. There should be little question that there actually was a decrease of Global mean OLR on the order of

0.075 W/m^2/yr over the time period September 2002 through June 2010, and that the majority of the decrease occurred in the tropics.

This result, found by both CERES and AIRS, should not be taken as indicative in any way as to what will happen in the future. It mainly shows that OLR anomalies and their Average Rates of Change can be determined very accurately by two totally independent instrumental and theoretical approaches. The agreement of anomaly time series of OLR as observed by CERES and computed from AIRS derived products also indirectly validates the anomaly time series of the AIRS derived products used in the computation of AIRS OLR. Moreover, it further indicates that anomaly time series of AIRS derived products can be used to explain the factors contributing to anomaly time series of OLR. This section of the paper uses the anomaly time series of the AIRS derived products and their ARC's over the extended time period September 2002 – April 2011 to explain the factors contributing to the anomaly time series of OLR and OLR_{CLR} over that time period.

Figure 11a shows the spatial distribution of the Average Rate of Change of the AIRS Version 5 surface skin temperature over the period September 2002 – April 2011. A number of important features are found in Figure 11a. While the global mean surface skin temperature ARC is essentially zero over this time period, there are areas where significant positive and negative T_{skin} ARC's exist. Both polar regions have been warming over this time period, especially near the North Pole. There is considerable warming and cooling structure in areas over Northern Hemisphere extra-tropical land, and there has been substantial cooling over much of Africa, especially south of 15°S, as well as over much of Australia. The tropics are marked by a substantial oceanic cooling

over the region 15°N to 15°S and 140°W longitude westward to 160°E which we will refer to as the AIRS El Niño region. The AIRS El Niño region, indicated by the green rectangle in Figure 11a, was defined to encompass the region of large negative sea surface temperature ARC's shown in the figure. There has also been substantial oceanic warming over this time period in the areas to the south, west, and north of the AIRS El Niño region. The AIRS El Niño region as defined in this paper is similar to the commonly used Niño 4 region, 5°N - 5°S, 120°W westward to 170°W (Yeh, et al. 2009).

Figure 11b shows the global distribution of ARC's of 500 mb specific humidity (%/yr) over the time period September 2002 to April 2011. OLR is very sensitive to the concentration of mid-upper tropospheric water vapor in very moist (i.e. tropical) areas, in the sense that increasing water vapor concentration increases atmospheric absorption in some spectral regions and therefore lowers OLR, everything else being equal. The area of strong equatorial surface temperature cooling between 160°E and 140°W, shown in Figure 11a, called the AIRS El Niño region, is marked by a significant mid-tropospheric drying during this period, and the surrounding areas of warming surface skin temperature are marked by considerable mid-tropospheric moistening during the period under study. There is also considerable mid-tropospheric moistening from 8°N to 20°S in the Atlantic Ocean and especially in the Eastern Pacific Ocean over this time period in areas where there has been at most a very small increase in surface skin temperature. In all of these regions, the changes in atmospheric water vapor, rather than in surface skin temperature, have been more significant contributors to the ARC's of AIRS OLR and OLR_{CLR} over the extended time period September 2002 – April 2011, shown in Figures 11c and 11d. Figures 11b-11d all contain the boundaries of OLR

Regions 1 and 2 defined previously. OLR Regions 1 and 2 both correspond to locations in which there has been considerable mid-tropospheric moistening over this time period, as well as considerable decreases in both OLR and OLR_{CLR}. Figures 11c and 11d are similar to, but different than, Figures 7a and 8a which show analogous ARC's computed over the shorter time period extending only to June 2010. As stated previously, the AIRS global mean ARC's of OLR and OLR_{CLR} over the extended time period are -0.093 $W/m^2/yr$ and -0.018 $W/m^2/yr$ respectively. Both values are considerably more negative than they were over the shorter time period as a result of inclusion of the latest La Niña time period during which there were substantial negative global mean anomalies of OLR and OLR_{CLR}.

Figures 11c and 11d show that the spatial distribution of ARC's of AIRS OLR and OLR_{CLR} over extra-tropical land areas closely track those of T_{skin} with areas of warming skin temperatures corresponding to areas of increasing OLR and OLR_{CLR} and vice versa for cooling areas. This demonstrates the expected result that a warming surface should result in increasing flux to space, all other things being held constant.

The spatial relationship between ARC's of OLR and T_{skin} in the tropics is quite different than in the extra-tropics, especially over ocean. There has been a significant equatorial cooling between September 2002 and April 2011 in the El Niño region surrounding the equator from 160°E eastward to 140°W. This is a reflection of the fact that the time period under study started with an El Niño event in 2002, and had La Niña events in 2007 and 2010. This change from El Niño conditions to La Niña conditions is the driving force behind the recent negative global mean and tropical mean OLR ARC's. The AIRS El Niño region of T_{skin} cooling is marked by significant increases in both OLR

and OLR_{CLR}. This region is surrounded to the north, south, and west by areas of oceanic warming. All of these oceanic areas are marked by large negative OLR ARC's. It is extremely important to note that equatorial OLR also shows large negative ARC's over OLR Region 1, 8°N to 20°S, 140°W eastward to 10°E, in which there are no spatially coherent changes with regard to T_{skin}.

Figure 11d shows that spatial ARC's of clear sky OLR, which to first order are independent of changes in cloud cover, closely match ARC's of OLR poleward of 60° both in phase and magnitude. This shows that OLR ARC's at high latitudes are not influenced substantially by changes in cloud cover $\alpha\epsilon$. In the tropics, the patterns of the ARC's of OLR and clear sky OLR are also similar to each other, but the magnitudes of the relative ARC's are substantially larger with regard to OLR than OLR_{CLR}. Tropical OLR_{CLR} ARC's are dominated by those of 500 mb specific humidity q_{500}. Tropical OLR ARC's are also affected by changes in water vapor, but are dominated primarily by those of cloud cover $\alpha\epsilon$. ARC's of fractional cloud cover (not shown) closely match those of 500 mb specific humidity. It is the combination of the effects of anomalies and trends of both tropospheric water vapor and fractional cloud cover that give rise to the anomalies and ARC's of OLR as observed by CERES and confirmed by AIRS.

Table 3 shows the spatial correlation of ARC's of OLR, OLR_{CLR}, $\alpha\epsilon$, q_{500}, and T_{skin} over the time period September 2002 through April 2011. Spatial correlations of ARC's of these quantities over the latitudinal domain 60°N through 90°N are shown above the diagonal in bold, and analogous spatial correlations over the latitudinal domain 15°N through 15°S are shown below the diagonal. At high latitudes, shown in bold, ARC's of OLR and OLR_{CLR} have a spatial correlation of 0.83 with each other. Both sets of ARC's

are also highly positively correlated with those of T_{skin}, especially OLR_{CLR}. At high latitudes, ARC's of specific humidity and fractional cloud cover are not highly correlated with each other or with any of the other geophysical parameters shown in the table.

Spatial correlations of ARC's of the same geophysical parameters in the tropics, shown below the diagonal, are very different from those at high latitudes. The correlations of ARC's of OLR and OLR_{CLR} in the tropics is again very high (0.80). In the North Polar region, the high correlation of ARC's of OLR and OLR_{CLR} arose because the spatial distribution of ARC's of OLR and OLR_{CLR} were both highly positively correlated with those of T_{skin}. In the tropics, this high correlation of OLR and OLR_{CLR} arises because both are highly negatively correlated with ARC's of fractional cloud cover $\alpha\epsilon$ and 500 mb specific humidity q_{500}. Unlike at high latitudes, ARC's of tropical T_{skin} are not highly correlated with those of any other of the geophysical parameters studied. Tropical correlations of ARC's and OLR and OLR_{CLR} with those of T_{skin} are actually somewhat negative because tropical correlations of T_{skin} with those of $\alpha\epsilon$ and q_{500} are somewhat positive. The high correlation of ARC's of OLR_{CLR} with those of $\alpha\epsilon$, on which OLR_{CLR} does not depend, arises because ARC's of $\alpha\epsilon$ and q_{500} are themselves highly positively correlated with each other.

Figure 12a shows the Hovmöller diagram of monthly mean T_{skin} anomalies for the period September 2002 through April 2011. The vertical green lines delineate the longitudinal band included in the El Niño region, 160°E longitude eastward to 140°W longitude. The largest SST anomalies tend to occur on either side of the dateline between these longitudinal limits. Figure 12a demonstrates that the large negative SST ARC near the equator extending from about 160°E eastward to 140°W is the result of

the transition from an El Niño at the end of 2002 to La Niñas over the time periods late 2007 through 2008, and especially late 2010 through early 2011. Equatorial T_{skin} anomalies between 100°E and 140°E tend to be smaller than, and of opposite sign to, those in the vicinity of the dateline. This gives rise to the band of weaker positive SST ARC's near the equator from 100°E to 140°E.

Figure 12b shows the Hovmöller diagram of 500 mb specific humidity. The vertical gray lines delineate the longitudinal extent of OLR Region 1, extending from 140°W eastward to 10°E. 500 mb specific humidity anomalies near the dateline in general follow those of SST very closely both in magnitude and in phase. This results from the fact that positive SST anomalies in the El Niño region correspond to periods of increased convection in that area, leading to enhanced moisture of the mid-troposphere. Conversely, negative SST anomalies in the El Niño area correspond to periods of decreased convection (increased subsidence) leading to periods of a drier mid-troposphere. Water vapor anomalies over Indonesia, from roughly 100°E to 140°E, are not only out of phase with those near the dateline, as are those of T_{skin}, but are also of comparable magnitude to water vapor anomalies near the dateline. This is the result of the westward shift of the area of maximum convection during La Niña periods from the dateline to Indonesia. This out of phase relationship gives rise to the very substantial positive ARC of 500 mb specific humidity over Indonesia during this time period, as shown in Figure 11b.

Figure 11b also shows substantial positive q_{500} ARC's in some tropical locations in which no significant changes in T_{skin} exist. The most notable of these is off the west coast of South America, in the vicinity of 8°N to 20°S from 140°W eastward to 80° W,

which is a part of OLR Region 1. There is also another region of positive q_{500} ARC's near the equator going across South America and extending eastward along the Atlantic Ocean to about 10°E longitude, also contained within OLR Region 1. Figure 12b shows that equatorial water vapor anomalies off the west coast of South America tend to be out of phase with those at the dateline, especially during the large La Niña events in 2007-2008 and 2010-2011. This indicates that La Niña periods of decreased convection near the dateline correspond to periods of increased convection eastward of 140°E, which is the result of the eastward shift of the convective branch of the Walker circulation during La Niña periods (Power and Smith 2007; Zhou et al. 2011). The same relationship is found to a lesser extent over the Atlantic Ocean extending to 10°E longitude at the eastern end of OLR Region 1.

Figure 12c shows the Hovmöller diagram of the AIRS effective cloud fraction. The anomalies of effective cloud fraction averaged over 5°N to 5°S latitude are closely in phase with those of 500 mb specific humidity, with a temporal/spatial correlation of 0.717. This correlation is a result of the fact that periods of increased convection (or subsidence) correspond to increases (or decreases) of not only mid-tropospheric water vapor but also cloud cover, especially with regard to high clouds. Anomalies of OLR_{CLR} are driven primarily by those of q_{500}, and those of OLR are driven primarily by effective cloud fraction, $\alpha\epsilon$, with a smaller contribution from q_{500}. The high correlation between tropical anomalies of OLR and OLR_{CLR} are the result of the correlation between anomalies of $\alpha\epsilon$ and q_{500}.

Table 4 shows the spatial-temporal correlations of the Hovmöller diagrams of anomalies of OLR, OLR_{CLR}, $\alpha\epsilon$, q_{500}, and T_{skin} derived from AIRS observations over the

period September 2002 through April 2011. Unlike Table 3, this table is symmetric above and below the diagonal because only one set of correlation statistics is presented. Spatial-temporal anomaly correlations between OLR, OLR_{CLR}, $\alpha\epsilon$, q_{500}, and T_{skin} averaged over the latitude range 5°N through 5°S are extremely close to those shown in the lower half of Table 3, representing spatial correlations of ARC's of these geophysical parameters in the tropics. This shows that not only are the spatial patterns of Average Rates of Change of tropical OLR, OLR_{CLR}, $\alpha\epsilon$, and q_{500} highly correlated with each other, but the detailed structure of their spatial anomalies as a function of time are also highly correlated.

7. Attribution of Recent Decreases in Global and Tropical Mean OLR to Changes Contained within OLR Regions 1 and 2

Figure 11c shows that the largest OLR ARC's occur in the tropics over a region covering Indonesia on the one hand, and near the dateline on the other. OLR ARC's in these areas are roughly equal to each other and of opposite sign, as are the OLR anomalies shown in Figure 9a. The effects of the large positive and negative tropical OLR ARC's near the dateline and over Indonesia tend to cancel in the zonal mean sense. As shown in Figure 6a, the negative tropical mean ARC comes primarily from the latitudinal range 8°N to 20°S. This in turn originates primarily from the subset of the tropics contained within Region 1, 8°N through 20°S and 140°W eastward to 10°E, outlined in Figures 11b-d. Analogous results are found in Figure 6b with regard to zonal mean ARC's of OLR_{CLR}.

Figure 13a shows the AIRS OLR anomaly time series averaged over OLR Region 1 in dark blue. Figure 13a also includes in black the El Niño index, this time

multiplied by 4, rather than multiplied by 3 as was done in Figure 4b. The Region 1 OLR anomaly time series closely follows that of the El Niño index, but is lagged in time (El Niño occurs first) by about 3 months. Therefore, in Figure 13a, Region 1 OLR anomalies are plotted 3 months earlier than they actually occurred. For this reason, the dark blue line starts 3 months before the black line, and also ends 3 months earlier than the black line. The correlation coefficient of the 3 month lagged Region 1 OLR anomaly with that of the El Niño index is 0.898. Figure 13a also contains the anomaly time series of OLR_{CLR} averaged over Region 1, shown by the light blue line, which like the dark blue line is lagged 3 months from the El Niño index. OLR_{CLR} anomalies in Region 1 are smaller than those of OLR, but are highly correlated with those of OLR, with a correlation coefficient of 0.873. The 3 month lagged OLR_{CLR} anomalies are also highly correlated with those of the El Nino index, with a correlation of 0.821.

The OLR and OLR_{CLR} anomalies averaged over OLR Region 1 are considerably larger than corresponding tropical mean anomalies shown in Figures 4b and 5b. Consequently the negative ARC's of OLR and OLR_{CLR} averaged over OLR Region 1, which are -0.530 W/m^{2}yr and -0.150 W/m^2/yr respectively, are considerably larger than the corresponding negative ARC's of tropical mean OLR and OLR_{CLR} given by -0.188 W/m^2/yr and -0.074 W/m^2/yr. These values are included in Table 5, which shows area mean Average Rates of Change of the AIRS anomaly time series of OLR and OLR_{CLR}, computed over the time period September 2002 through April 2011, averaged over different spatial domains.

The negative tropical mean OLR ARC over the period September 2002 through April 2011 computed as previously, but after replacing OLR ARC's in OLR Region 1 by

zeroes, is reduced from -0.188 W/m^2/yr to -0.032 W/m^2/yr, and the negative global mean OLR ARC is reduced from -0.093 W/m^2/yr to -0.039 W/m^2/yr. When an analogous procedure is done with regard to OLR_{CLR}, the negative tropical mean OLR_{CLR} ARC is reduced from -0.074 W/m^2/yr to -0.030 W/m^2/yr and the negative global mean ARC of OLR_{CLR} is reduced from -0.018 W/m^2/yr to -0.003 W/m^2/yr. This indicates that a large part of the recent negative global mean and tropical mean OLR and OLR_{CLR} ARC's results from the contribution of OLR and OLR_{CLR} anomalies within OLR Region 1. These anomalies are in turn in phase with the El Niño index, but lagged in time by roughly 3 months. It is for this reason that the global and tropical OLR and OLR_{CLR} anomaly time-series shown in Figures 4 and Figure 5 are in phase with, and highly correlated with, El Niño/La Niña activity as noted earlier.

Figures 11c and 11d also show that there are substantial negative ARC's of OLR and OLR_{CLR} within the rectangular box surrounding the area from 15°S to 30°S and westward from 150°W to 140°E, referred to as OLR Region 2. One-third of this region is in the tropics and the remaining two-thirds is in the subtropics. OLR Region 2 is also marked by large positive ARC's of mid-tropospheric water vapor, as shown in Figure 11b, and cloud cover (not shown) over the period under study. Figure 13b shows in dark blue and light blue the time series of OLR anomalies and OLR_{CLR} anomalies in OLR Region 2, superimposed on the time series of the El Niño index, this time multiplied by 10, without a time lag. As shown in Table 5, OLR in Region 2 has an extremely large negative ARC of -1.74 W/m^2/yr, and OLR_{CLR} in Region 2 has a very large negative ARC of -0.54 W/m^2/yr. All three curves in Figure 13b are highly correlated with each other in time. The correlation between the unlagged anomaly time series of the El Niño index

and OLR in region 2 is 0.854, the correlation between the El Niño index and the anomaly time series of OLR_{CLR} in Region 2 is 0.781, and the correlation between the anomaly time series of OLR and OLR_{CLR} in region 2 is 0.936. As shown in Table 5, the ARC's of global and tropical mean OLR and OLR_{CLR}, computed after zeroing out OLR and OLR_{CLR} ARC's in both OLR Region 1 and OLR Region 2, are reduced to essentially zero. This shows that the large negative global and tropical ARC's of OLR and OLR_{CLR} over the period September 2002 through April 2011 can be attributed almost completely to temporal changes in mid-tropospheric water vapor and cloud cover that have taken place primarily within OLR Region 1 along the equator in the eastern Pacific and Atlantic Ocean, with a further contribution from OLR Region 2 primarily in the southern hemisphere subtropics south-southwest of the El Niño region, covering Eastern Australia and parts of the southwestern Pacific Ocean.

References:

Allan, R. P., and M. A. Ringer, 2003: Inconsistencies between satellite estimates of longwave cloud forcing and dynamical fields from reanalyzes. *Geophys. Res. Lett.*, **30,** 4.

Barkstrom, B., E. Harrison, G. Smith, R. Green, J. Kibler, R. Cess, the ERBE Science Team,1989: Earth Radiation Budget (ERBE) Archival and April 1985 Results. *Bulletin of the American Meteorological Society*, **70**, 1254-1262.

Barlow, M., M. Wheeler, B. Lyon, and H. Cullen, 2005: Modulation of Daily Precipitation over Southwest Asia by the Madden-Julian Oscillation. *Mon. Weather Rev.*, **133,** 3579-3594.

Brown, J. R., S. B. Power, F. P. Delage, R. A. Colman, A. F. Moise, B. F. Murphy, 2011: Evaluation of the South Pacific Convergence Zone in IPCC AR4 Climate Model Simulations of the Twentieth Century. *J. Climate*, **24**, 1565-1582. doi:10.1175/2010JCLI3942.1.

Chiodi, A. M., and D. E. Harrison, 2010: Characterizing Warm-ENSO Variability in the Equatorial Pacific: An OLR Perspective. *J. Clim.*, **23,** 2428-2439.

Chu, P. S., and J. B. Wang, 1997: Recent Climate Change in the Tropical Western Pacific and Indian Ocean Regions as Detected by Outgoing Longwave Radiation Records. *J. Clim.*, **10,** 636-646.

Chung, E. S., D. Yeomans, and B. J. Soden, 2010: An assessment of climate feedback processes using satellite observations of clear-sky OLR. *Geophys. Res. Lett.*, **37,** 7.

Clement, A. C., B. Soden, 2005: The Sensitivity of the Tropical-Mean Radiation Budget. *J. Climate*, **18**, 3189-3203. doi: 10.1175/JCLI3456.1.

Dessler, A. E., Z. Zhang, and P. Yang, 2008: Water-vapor climate feedback inferred from climate fluctuations, 2003-2008. *Geophys. Res. Lett*., **35**, L20704, doi: 10.1029/2008GL035333.

Dessler, A. E., 2010: A Determination of the Cloud Feedback from Climate Variations over the Past Decade. *Science*, **330**, 1523-1527. doi: *10.1126/science.1192546*

Fasullo, J. T., and K. E. Trenberth, 2008: The Annual Cycle of the Energy Budget. Part II: Meridional Structures and Poleward Transports. *J. Clim.*, **21,** 2313-2325.

Folland, C. K., J. A. Renwick, M. J. Salinger, and A. B. Mullan, 2002: Relative influences of the Interdecadal Pacific Oscillation and ENSO on the South Pacific Convergence Zone. *Geophys. Res. Lett*., **29**, 13 doi:10.1029/2001GL014201.

Gruber, A., R. Ellingson, P. Ardanuy, M. Weiss, S. K. Yang, and S. N. Oh, 1994: A Comparison of ERBE and AVHRR Longwave Flux Estimates. *Bulletin of the American Meteorological Society*, **75,** 2115-2130.

Hoyos, C. D., and P. J. Webster, 2007: The Role of Intraseasonal Variability in the Nature of Asian Monsoon Precipitation. *J. Clim.*, **20,** 4402-4424.

Huang, Y., and V. Ramaswamy, 2009: Evolution and Trend of the Outgoing Longwave Radiation Spectrum. *J. Clim.*, **22,** 4637-4651. doi: 10.1175/2009JCLI2874.1

Iacono, M. J., J. S. Delamere. E. J. Mlawer, M. W. Shephard, S. A. Clough, and W. D. Collins, 2008: Radiative Forcing by Long-Lived Greenhouse Gases: Calculations with the AER Radiative Transfer Models. *J. Geophys. Res*., **113**, D13103, doi:10.1029/2008JD009944.

Jacobowitz, H., H. V. Soule, H. L. Kyle, F. B. House, and the Nimbus 7 ERB Experiment Team, 1984: The Earth Radiation Budget (ERB) Experiment: An Overview. *J. Geophys. Res*., **89**, 5021-5038, doi:10.1029/JD089iD04p05021.

Jones, C., L. M. V. Carvalho, R. W. Higgins, D. E. Waliser, and J. K. E. Schemm, 2004: Climatology of Tropical Intraseasonal Convective Anomalies: 1979-2002. *J. Clim.*, **17,** 523-539.

Kidson, J. W., M. J. Revell, B. Bhaskaran, A. B. Mullan, and J. A. Renwick, 2002: Convection Patterns in the Tropical Pacific and Their Influence on the Atmospheric Circulation at Higher Latitudes. *J. Clim.*, **15,** 137-159.

Kiladis, G. N., K. H. Straub, and P. T. Haertel, 2005: Zonal and Vertical Structure of the Madden-Julian Oscillation. *Journal of the Atmospheric Sciences*, **62,** 2790-2809.

Kyle, H. L., A. Arking, J. R. Hickey, P. E. Ardanuy, H. Jacobowitz, H. Jacobowitz, L. L. Stowe, G. G. Campbell, T. Vonder Haar, F. B. House, R. Maschhoff, and G. L. Smith, 1993: The Nimbus Earth Radiation Budget (ERB) Experiment: 1975-1992. *Bull. Am. Meteorol*. *Soc*., **74**, 815-830.

Loeb, N. G., S. Kato, W. Su, T. Wong, F. Rose, D. Doelling, J. Norris, 2011: Advances in Understanding Top-of-Atmosphere Radiation Variability from Satellite Observations. *Surveys in Geophysics* (submitted).

Loeb, N. G., S. Kato, K. Loukachine, and N. Manalo-Smith, 2005: Angular Distribution Models for Top-of-Atmosphere Radiative Flux Estimation from the Clouds and the Earth's Radiant Energy System Instrument on the *Terra* Satellite. Part 1: Methodology. *J. Atmos. Ocean. Tech*., **22**(4), 338-351.doi:10.1175/JTECH1712.1.

McClatchey, R. A., R. W. Fenn, J. E. A. Selby, F. E. Volz, and J. S. Garing, 1972: Optical Properties of the Atmosphere (Third Edition). *Environ. Res. Papers*, **411**, AFCRL, Bedford, MA, 108 pp.

Mehta, A. V. and J. Susskind, 1999a: Outgoing Longwave Radiation from the TOVS Pathfinder Path A Data Set. *J. of Geophys. Res*., **104**, 12193-12212.

Mehta, A. V. and J. Susskind, 1999b: Longwave Radiative Flux Calculations in the TOVS Pathfinder Path A Data Set. *NASA Tech. Rep., GSFC/CR-1999-208643*.
Proc. SPIE International Symp. Infrared Spaceborne Remote Sensing and Instrumentation XVII, San Diego, CA, August 2009.

Minnis, P., Q. Z. Trepte, S. Sun-Mack, Y. Chen, D. R. Doelling, et al., 2008: Cloud Detection in Non-polar Regions for CERES Using TRMM VIRS and Terra and Aqua MODIS Data. *IEEE Trans. Geosci. Remote Sens*., **46**, 3857-3884.

Minnis, P., S. Sun-Mack, D. F. Young, P. W. Heck, D. P. Garber, et al., 2011: CERES Edition-2 Cloud Property Retrievals Using TRMM VIRS and Terra and Aqua MODIS data. Part 1: Algorithms. *IEEE Trans. Geosci. Remote Sens*. (in press).

Power, S. B., and I. N. Smith, 2007: Weakening of the Walker Circulation and apparent dominance of El Niño both reach record levels, but has ENSO really changed?, *Geophys. Res. Lett*., **34**, L18702, doi:10.1029/2007GL030854.

Soden, B. J., and I. M. Held, 2006: An Assessment of Climate Feedbacks in Coupled Ocean–Atmosphere Models. *J. Clim.*, **19,** 3354-3360.

Soden, B. J., I. M. Held, R. Colman, K. M. Shell, J. F. Kiehl, C. A. Shields, 2008: Quantifying Climate Feedbacks Using Radiative Kernels. *J. Clim*., **21**, 3504-3520.

Susskind, J. and J. E. Searl, 1978: Synthetic Atmospheric Transmittance Spectra Near 15 μm and 4.3 μm. *J. Quant. Spectr. Rad. Trans*., **19**, 195-215.

Susskind, J., P. Piraino, L. Rokke, L. Iredell, and A. V. Mehta, 1997: Characteristics of the TOVS Pathfinder Path A Data Set. *Bull. of Amer. Meteorol. Soc*., **78**, 1449-1472.

Susskind, J., C.D. Barnet, J.M. Blaisdell, 2003: Retrieval of atmospheric and surface parameters from AIRS/AMSU/HSB data in the presence of clouds. IEEE Transactions on Geoscience and Remote Sensing, Issue 2, **41**, doi: 10.1109/TGRS.2002.808236, 390-409.

Susskind, J., J. Blaisdell, and L. Iredell, 2009: Improved Determination of Surface and Atmospheric Temperatures Using Only Shortwave AIRS Channels. *Proc. SPIE International Symp. Infrared Spaceborne Remote Sensing and Instrumentation XVII*, San Diego, CA, August 2009.

Susskind, J., J. M. Blaisdell, L. Iredell, and F. Keita, 2011a: Improved Temperature Sounding and Quality Control Methodology Using AIRS/AMSU Data: The AIRS Science Team Version 5 Retrieval Algorithm. Geoscience and Remote Sensing, IEEE Transactions on Geoscience and Remote Sensing, Issue: 99 Digital Object Identifier: 10.1109/TGRS.2010.2070508, Publication Year: 2011, 1-25.

Susskind, J., G. Molnar, and L. Iredell, 2011b: The Effect of El Niño/La Niña Oscillations on Recent Anomaly Time Series of OLR. Submitted to *J. Climate*.

Trenberth, E. T., J. T. Fasullo, C. O'Dell, and T. Wong, 2010: Relationships between tropical sea surface temperature and top-of-atmosphere radiation. *Geophys. Res. Lett*., **37**, L03702, doi:10.1029/2009GL042314.

Wielicki, B. A., B. R. Barkstrom, E. F. Harrison, R. B. Lee III, G. L. Smith, and J. E. Cooper, 1996: Clouds and the Earth's Radiant Energy System (CERES): An Earth Observing System Experiment. *Bull. Amer. Meteor. Soc*., **77**, 853-868.

Wong, T., B. A. Wielicki, R. B. Lee, III, G. L. Smith, K. A. Bush, J. K. Willis, 2006: Reexamination of the Observed Decadal Variability of the Earth Radiation Budget Using Altitude-Corrected ERBE/ERBS Nonscanner WFOV Data. *J. Climate*, **19**, 4028-4040.

Yeh, S.-W., J.-S. Kug, B. Dewitte, M.-H. Kwon, B. P. Kirtman, and F.-F. Jin, 2009: El Niño in a changing climate. *Nature*, **461**, 511-514, doi:10.1038/nature08316.

Young, D. F., P. Minnis, D. R. Doelling, G. G. Gibson, and T. Wong, 1998: Temporal Interpolation Methods for the Clouds and the Earth's Radiant Energy System (CERES) Experiment. *Jour. of Applied Meteor*., **37**(6), 572-590.

Zhou, Y. P., K.-M. Xu, Y. C. Sud, and A. K. Betts, 2011: Recent Trends of the Tropical Hydrological Cycle Inferred from Global Precipitation Climatology Project and International Satellite Cloud Climatology Project Data. *J. Geophys. Res*., **116**, D09101, doi: 10.1029/2010JD015197.

Table 1a. Comparison of Global OLR Time Series
September 2002 through August 2009

	AIRS Minus CERES Terra	AIRS Minus CERES Aqua	CERES Terra Minus CERES Aqua
Slope [W/m^2/yr]	-0.0195	-0.0690	-0.0495
Mean [W/m^2]	9.07	9.53	0.46
Standard Dev.[W/m^2]	0.345	0.475	0.243

Statistical comparisons of time series for the period September 2002 through August 2009 for AIRS minus CERES Terra OLR, AIRS minus CERES Aqua OLR, and CERES Terra minus CERES Aqua OLR. Shown are the slopes of the least squares linear fits, and mean differences and standard deviations of the different OLR time series.

Table 1b. Comparison of Global OLR_{CLR} Time Series
September 2002 through August 2009

	AIRS Minus CERES Terra	AIRS Minus CERES Aqua	CERES Terra Minus CERES Aqua
Slope [W/m^2/yr]	0.0475	0.0762	0.0287
Mean [W/m^2]	6.34	6.49	0.15
Standard Dev.[W/m^2]	0.325	0.339	0.513

Statistical comparisons of time series for the period September 2002 through August 2009 for AIRS minus CERES Terra OLR_{CLR}, AIRS minus CERES Aqua OLR_{CLR}, and CERES Terra minus CERES Aqua OLR_{CLR}. Shown are the slopes of the least squares linear fits, and mean differences and standard deviations of the different OLR time series.

Table 2a. OLR Anomaly Time Series Comparison
September 2002 through June 2010

Data Set	Global	Tropical
AIRS ARC ($W/m^2/yr$)	−0.0881 ± 0.0055	−0.1125 ± 0.0128
CERES Terra ARC ($W/m^2/yr$)	−0.0655 ± 0.0050	−0.1006 ± 0.0121
AIRS Minus CERES STD (W/m^2)	0.147	0.210
AIRS/CERES Correlation	0.953	0.983

Global and Tropical statistical comparisons of OLR anomaly time series for the period September 2002 through June 2010 for AIRS and CERES Terra OLR. Shown are the Average Rates of Change, the standard deviations between the anomaly time series, and the temporal correlations of the anomaly time series.

Table 2b. OLR_{CLR} Anomaly Time Series Comparison
September 2002 through June 2010

Data Set	Global	Tropical
AIRS ARC ($W/m^2/yr$)	−0.0045 ± 0.0036	−0.0177 ± 0.0067
CERES Terra ARC ($W/m^2/yr$)	−0.0703 ± 0.0043	−0.1018 ± 0.0078
AIRS Minus CERES STD (W/m^2)	0.195	0.273
AIRS/CERES Correlation	0.857	0.922

Global and Tropical statistical comparisons of OLR_{CLR} anomaly time series for the period September 2002 through June 2010 for AIRS and CERES Terra OLR_{CLR}. Shown are the Average Rates of Change, the standard deviations between the anomaly time series, and the temporal correlations of the anomaly time series.

Table 2c. Correlations between OLR and OLR_{CLR} Anomaly Time Series in Different Domains
AIRS and CERES

	Global OLR	Tropical OLR	Global OLR_{CLR}	Tropical OLR_{CLR}	El Niño Index
Global OLR	**---**	**0.56**	**0.77**	**0.48**	**0.47**
Tropical OLR	0.55	**---**	**0.51**	**0.87**	**0.69**
Global OLR_{CLR}	0.79	0.56	**---**	**0.65**	**0.46**
Tropical OLR_{CLR}	0.55	0.87	0.73	**---**	**0.63**
El Niño Index	0.41	0.68	0.52	0.70	**---**

Temporal correlations of AIRS and CERES OLR and OLR_{CLR} global and tropical anomaly time series. Correlations using AIRS data records are shown above the diagonal in bold and those using CERES data are shown beneath the diagonal.

Table 3. Spatial Correlations of ARC's of AIRS Derived Products over the Time Period September 2002 through April 2011
90˚N to 60˚N and 15˚N to 15˚S

	OLR	OLR_{CLR}	αϵ	q_{500}	T_{skin}
OLR	**---**	**0.83**	**0.07**	**0.23**	**0.77**
OLR_{CLR}	0.80	**---**	**0.43**	**0.36**	**0.91**
αϵ	-0.91	-0.80	**---**	**0.11**	**0.44**
q_{500}	-0.81	-0.82	0.69	**---**	**0.33**
T_{skin}	-0.45	-0.08	0.26	0.43	**---**

Spatial correlation of ARC's of AIRS derived products over the time period September 2002 through April 2011. Spatial correlation for the region 60˚ through 90˚N are shown in bold above the diagonal. Spatial correlations for the region 15˚N through 15˚S are shown beneath the diagonal.

Table 4. Spatial-temporal Correlations of AIRS Anomaly Hovmöller Diagrams 5˚N-5˚S September 2002 Through April 2011

	OLR	OLR_{CLR}	αϵ	q_{500}	T_{skin}
OLR	1.000	0.80	-0.93	-0.79	-0.45
OLR_{CLR}	0.80	1.000	-0.77	-0.72	-0.05
αϵ	-0.93	-0.77	1.000	072	0.30
q_{500}	-0.79	-0.72	0.72	1.000	0.53
T_{skin}	-0.45	-0.05	0.30	0.53	1.000

Spatial-temporal Correlations of AIRS Anomaly Hovmöller Diagrams 5 -5˚S September 2002 Through April 2011. Values above and below the diagonal represent the same phenomena and are equal to each other.

Table 5. Area Mean Average Rates of Change of OLR and OLR_{CLR} ($W/m^2/yr$) September 2002 through April 2011

Spatial Area	OLR	OLR_{CLR}
Global	-0.093 ± 0.0045	-0.018 ± 0.0031
Tropical	-0.188 ± 0.0111	-0.074 ± 0.0059
Region1	-0.530 ± 0.0229	-0.150 ± 0.0097
Region 2	-1.740 ± 0.0672	-0.540 ± 0.0218
Global excluding Region 1	-0.039 ± 0.0035	-0.003 ± 0.0026
Tropical excluding Region 1	-0.032 ± 0.0080	-0.030 ± 0.0038
Global excluding Region 1 and 2	-0.004 ± 0.0035	0.008 ± 0.0026
Tropical excluding Region 1 and 2	0.002 ± 0.0078	-0.018 ± 0.0035

Area mean Average Rates of Change of AIRS OLR and OLR_{CLR} anomaly time series over the period September 2002 through April 2011 computed over different spatial domains.

Figure and Table Captions

Figure 1a

Global monthly mean OLR from Version-5 AIRS and Edition-2.5 CERES aboard Aqua and Terra for the period September 2002 through April 2011.

Figure 1b

Global monthly mean OLR_{CLR} from Version-5 AIRS and Edition-2.5 CERES aboard Aqua and Terra for the period September 2002 through April 2011.

Figure 2a

Global monthly mean OLR differences among AIRS, CERES Terra, and CERES Aqua; and dashed line showing the average value of each OLR difference for the overlap periods between each data set.

Figure 2b

Global monthly mean OLR_{CLR} differences among AIRS, CERES Terra, and CERES Aqua; and dashed line showing the average value of each OLR_{CLR} difference for the overlap periods between each data set.

Figure 3a

The AIRS Science Team Version-6 OLR minus Version-5 OLR for the 1:30 AM/PM average of the seven day period, September 6, 2002, January 25, 2003, September 29, 2004, August 5, 2005, February 24, 2007, August 10, 2007, and May 30, 2010.

Figure 3b

The AIRS Science Team Version-6 OLR_{CLR} minus Version-5 OLR_{CLR} for the 1:30 AM/PM average of the same seven days.

Figure 4a

Global mean AIRS and CERES Terra monthly mean OLR anomaly time series and their anomaly differences for the overlap period September 2002 through June 2010.

Figure 4b

Tropical (20°N to 20°S) mean monthly mean OLR anomaly time series and anomaly differences of AIRS and CERES Terra for the overlap period September 2002 through June 2010. Also shown in black is the AIRS El Niño index multiplied by 3.

Figure 5a

Global mean monthly mean OLR_{CLR} anomaly time series and anomaly differences of AIRS and CERES Terra for the overlap period September 2002 through June 2010.

Figure 5b

Tropical (20°N to 20°S) mean monthly mean OLR_{CLR} anomaly time series and anomaly differences of AIRS and CERES Terra for the overlap period September 2002 through June 2010. Also shown in black is the AIRS El Niño index multiplied by 2.

Figure 6a

Zonal mean Average Rates of Change (ARC's) for AIRS and CERES Terra OLR monthly mean time series for the period September 2002 through June 2010, as well as the difference of the two sets of ARC's. The majority of the decrease in global OLR during this period originates in the tropics south of 8°N.

Figure 6b

Zonal mean ARC's for AIRS and CERES Terra OLR_{CLR} monthly mean time series for the period September 2002 through June 2010, as well as the difference of the two sets of ARC's.

Figure 7a

Spatial 1° latitude by 1° longitude distribution of global AIRS OLR ARC's over the time period September 2002 through June 2010. OLR Region 1 is outlined in gray and OLR Region 2 is outlined in black in this and most subsequent figures showing spatial distributions of ARC's of different parameters.

Figure 7b

Spatial 1° latitude by 1° longitude distribution of global CERES OLR ARC's over the time period September 2002 through June 2010.

Figure 7c

Spatial distribution of ARC's of AIRS minus CERES OLR.

Figure 8a

Spatial 1° latitude by 1° longitude distribution of global AIRS OLR_{CLR} ARC's over the time period September 2002 through June 2010.

Figure 8b

Spatial 1° latitude by 1° longitude distribution of global CERES OLR_{CLR} ARC's over the time period September 2002 through June 2010.

Figure 8c

Spatial distribution of ARC's of AIRS minus CERES OLR_{CLR}.

Figure 9a

Hovmöller diagram for time series of monthly mean AIRS OLR anomalies integrated over the latitude range 5°N through 5°S in each 1° longitude bin for the period September 2002 through April 2011. The longitudinal domain of OLR Region 1 is indicated by the gray vertical lines in this and most subsequent Hovmöller diagrams.

Figure 9b

Hovmöller diagram for time series of monthly mean CERES OLR anomalies integrated over the latitude range 5°N through 5°S in each 1° longitude bin for the period September 2002 through June 2010.

Figure 9c

Hovmöller diagram for the difference between AIRS OLR and CERES OLR.

Figure 10a

Hovmöller diagram for time series of monthly mean AIRS OLR_{CLR} anomalies integrated over the latitude range 5°N through 5°S in each 1° longitude bin for the period September 2002 through April 2011.

Figure 10b

Hovmöller diagram for time series of monthly mean CERES OLR_{CLR} anomalies integrated over the latitude range 5°N through 5°S in each 1° longitude bin for the period September 2002 through June 2010.

Figure 10c

Hovmöller diagram for the difference between AIRS OLR and CERES OLR_{CLR}

Figure 11a

Spatial distribution of Average Rate of Change of AIRS surface skin temperature (K/yr) over the period September 2002 through April 2011. The spatial domain of the AIRS El Niño region is outlined in green.

Figure 11b

Spatial distribution of Average Rate of Change of AIRS 500 mb specific humidity (%/yr) over the period September 2002 through April 2011.

Figure 11c

Spatial distribution of Average Rate of Change of AIRS OLR ($W/m^2/yr$) over the period September 2002 through April 2011.

Figure 11d

Spatial distribution of Average Rate of Change of AIRS Clear Sky OLR ($W/m^2/yr$) over the period September 2002 through April 2011.

Figure 12a

Hovmöller diagram of AIRS Surface Skin Temperature anomalies (K). The longitudinal domain of the El Niño region is enclosed between the green vertical lines.

Figure 12b

Hovmöller diagram of AIRS 500 mb specific humidity anomalies (%). The longitudinal domain of Region 1 is enclosed between the gray vertical lines.

Figure 12c

Hovmöller diagram of AIRS effective cloud fraction anomalies (%). The longitudinal domain of Region 1 is enclosed between the gray vertical lines.

Figure 13a

AIRS OLR and OLR_{CLR} anomaly time series averaged over OLR Region 1 superimposed on the AIRS El Niño index multiplied by 4 and plotted 3 months earlier.

Figure 13b

AIRS OLR and OLR_{CLR} anomaly time series averaged over OLR Region 2 superimposed on the AIRS El Niño index multiplied by 10 without a time lag.

Table 1

Statistical comparisons of anomaly time series for the period September 2002 through August 2009 for AIRS minus CERES Terra OLR, AIRS minus CERES Aqua OLR, and CERES Terra minus CERES Aqua OLR. Shown are the slopes of the least squares linear fits, and mean differences and standard deviations of the different OLR time series.

Table 2

Global and Tropical statistical comparisons of OLR anomaly time series for the period September 2002 through February 2010 for AIRS and CERES Terra OLR. Shown are the Average Rates of Change, the standard deviations between the anomaly time series, and the temporal correlations of the anomaly time series.

Table 3

Spatial correlation of ARC's of AIRS derived products over the time period September 2002 through April 2011. Spatial correlations for the region 60°N through 90°N are shown in bold above the diagonal. Spatial correlations for the region 15°N through 15°S are shown beneath the diagonal.

Table 4

Spatial-temporal correlations of AIRS anomaly Hovmöller Diagrams 5°N-5°S September 2002 through April 2011. Values above and below the diagonal represent the same phenomena and are equal to each other.

Table 5

Area mean Average Rates of Change of AIRS OLR and OLR_{CLR} anomaly time series over the period September 2002 through April 2011 computed over different spatial domains.

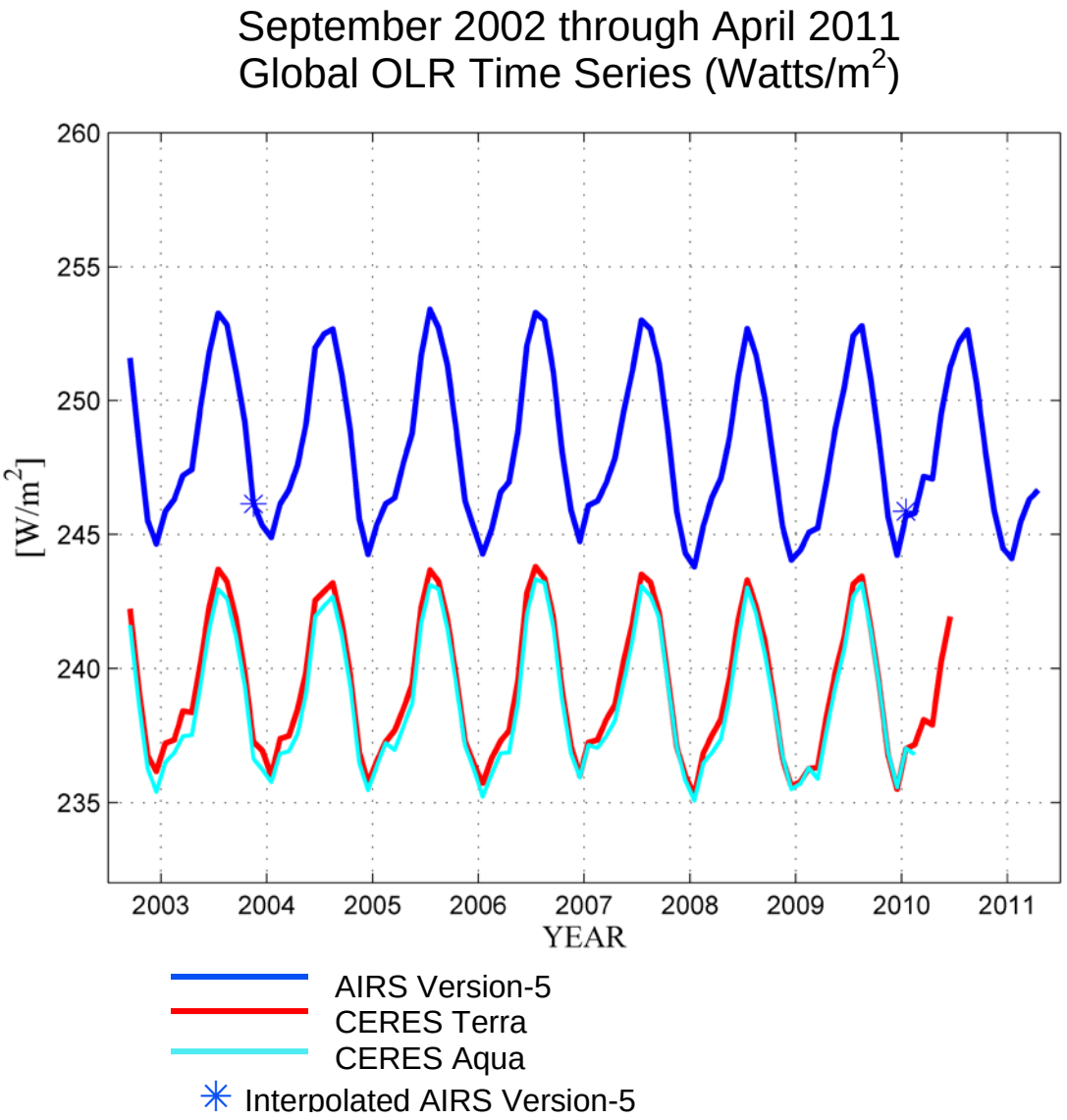

Figure 1a. Global monthly mean OLR from Version-5 AIRS and Edition-2.5 CERES aboard Aqua and Terra for the period September 2002 through April 2011.

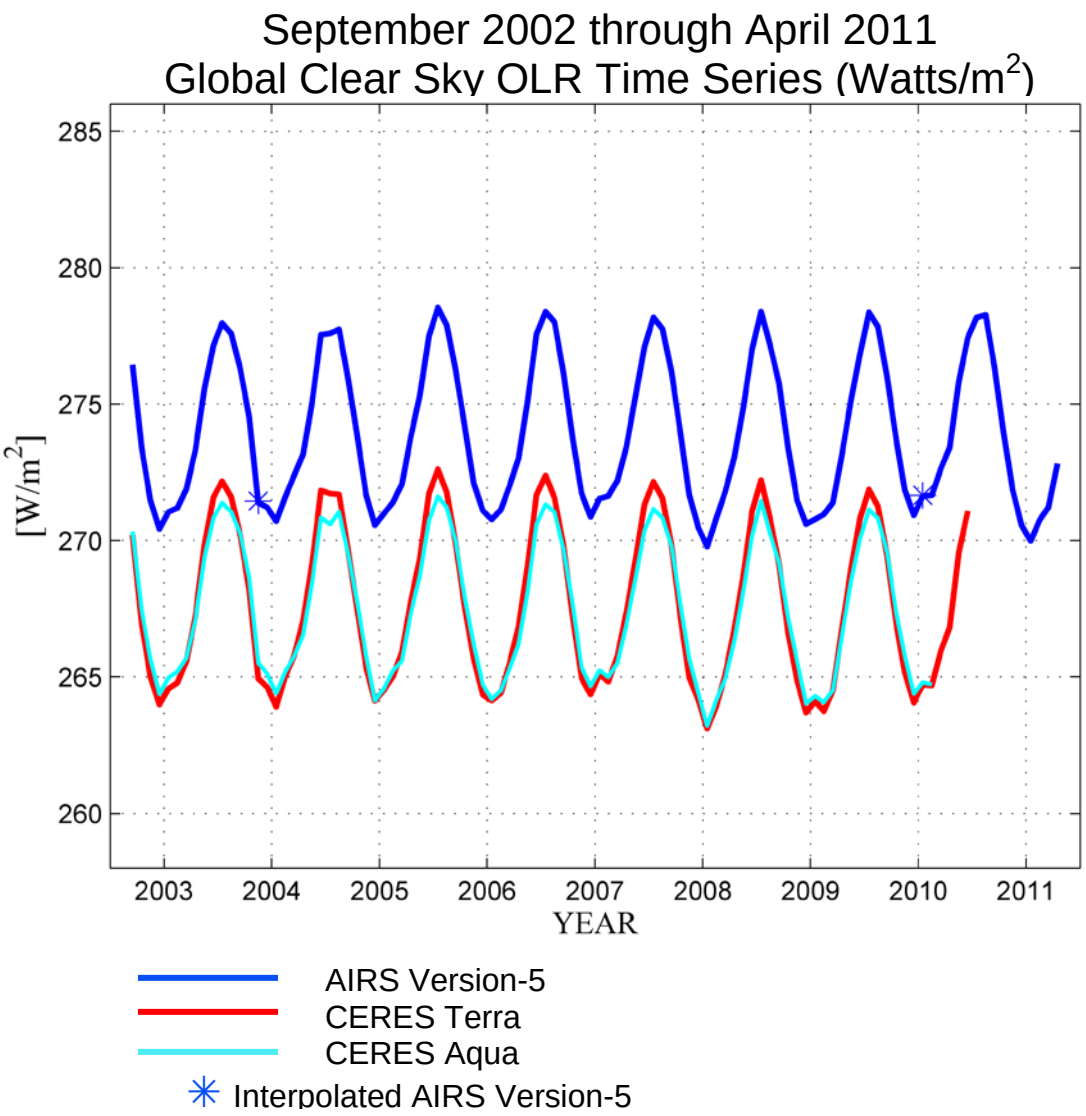

Figure 1b. Global monthly mean OLR_{CLR} from Version-5 AIRS and Edition-2.5 CERES aboard Aqua and Terra for the period September 2002 through April 2011.

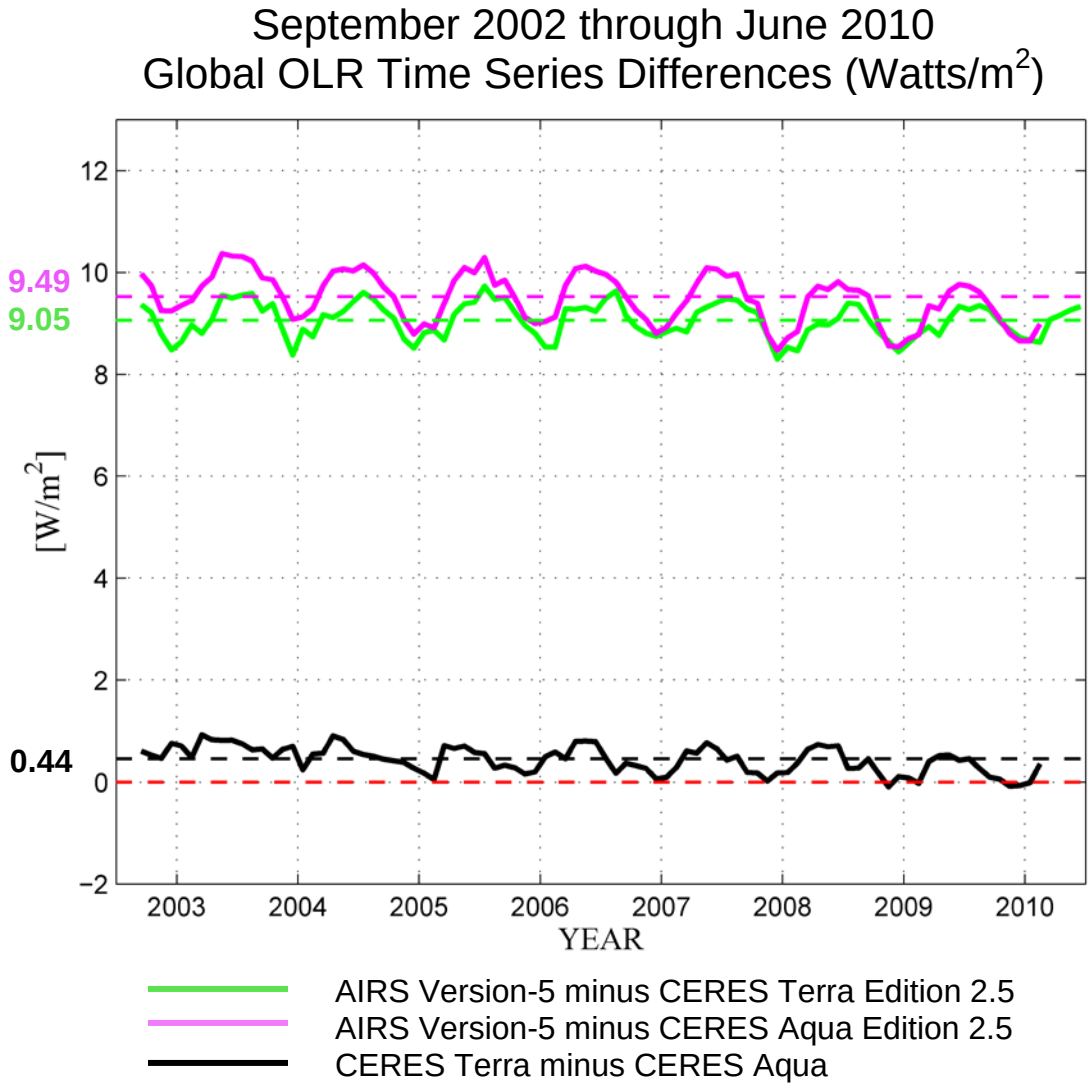

Figure 2a. Global monthly mean OLR differences among AIRS, CERES Terra, and CERES Aqua; and dashed line showing the average value of each OLR difference for the overlap periods between each data set.

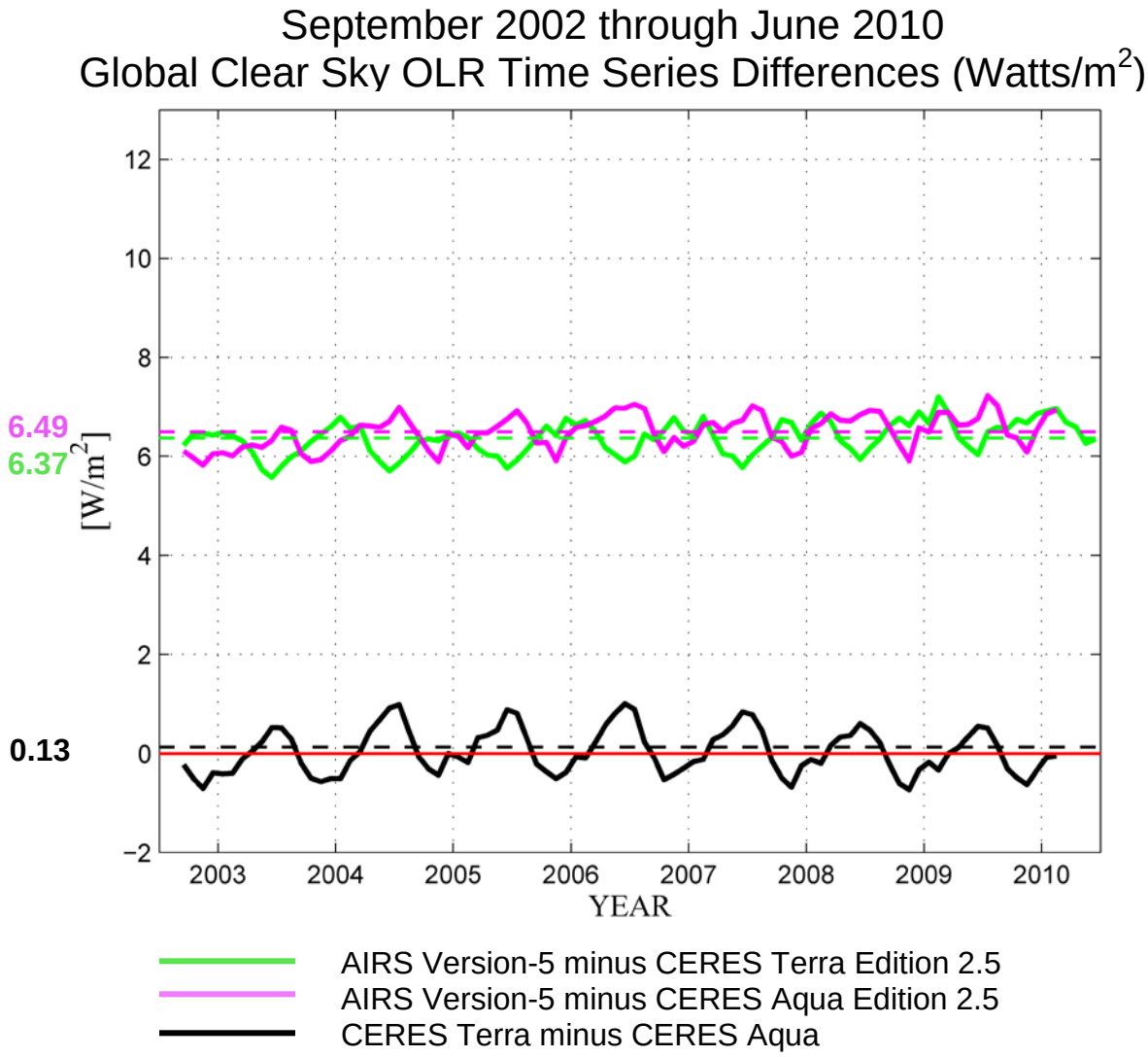

Figure 2b. Global monthly mean OLR_{CLR} differences among AIRS, CERES Terra, and CERES Aqua; and dashed line showing the average value of each OLR_{CLR} difference for the overlap periods between each data set.

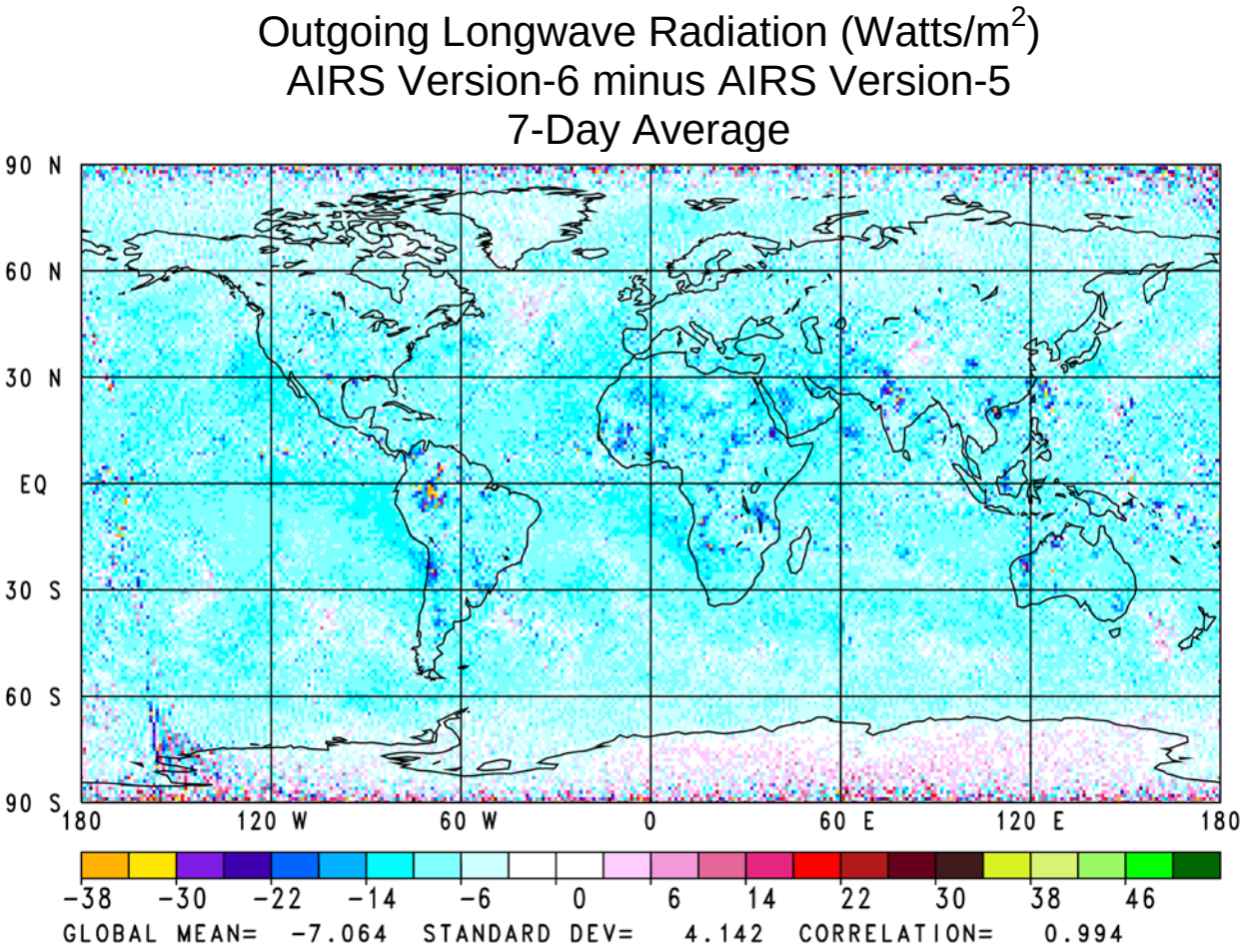

Figure 3a. The AIRS Science Team Version-6 OLR minus Version-5 OLR for the 1:30 AM/PM average of the seven day period, September 6, 2002, January 25, 2003, September 29, 2004, August 5, 2005, February 24, 2007, August 10, 2007, and May 30, 2010.

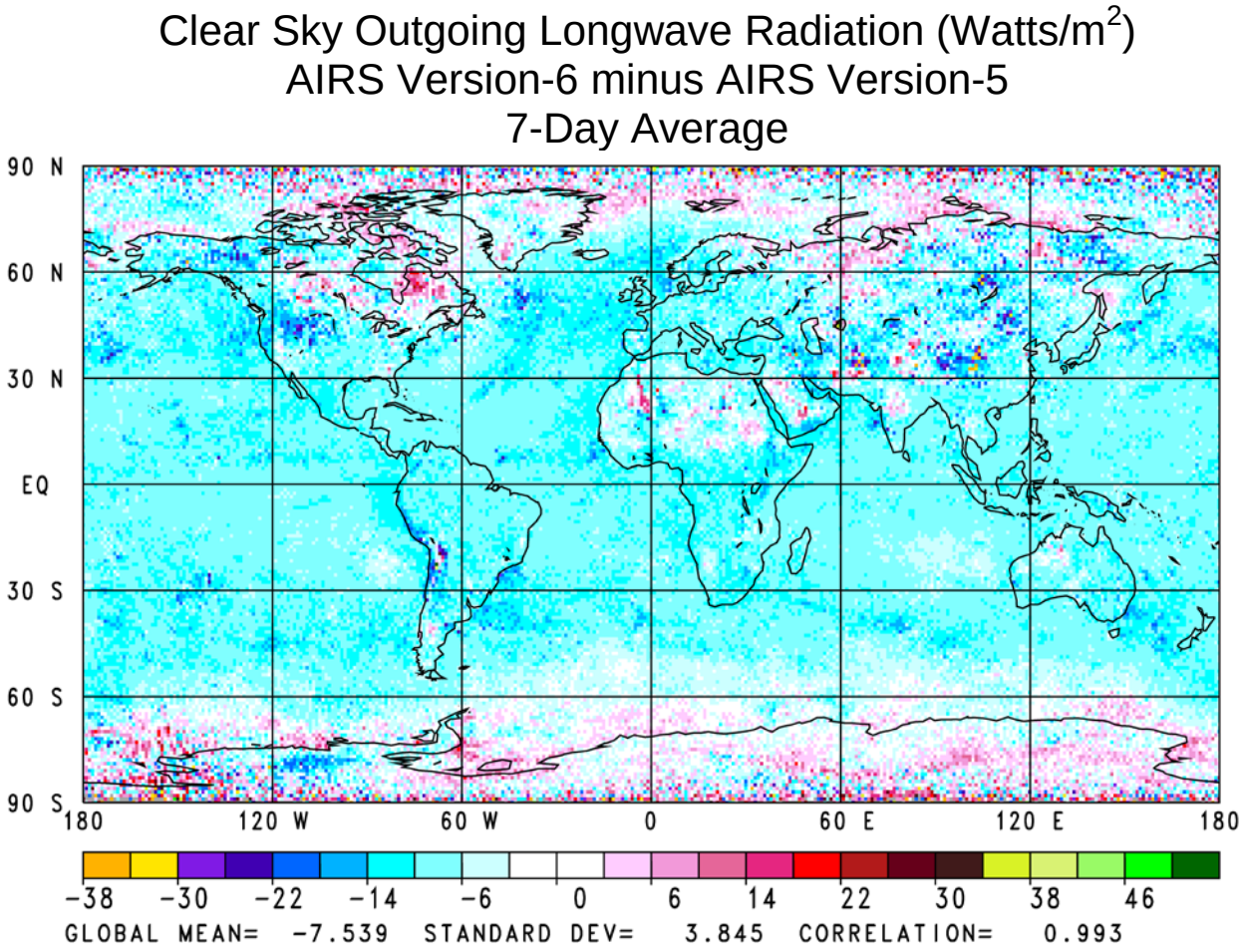

Figure 3b. The AIRS Science Team Version-6 OLR_{CLR} minus Version-5 OLR_{CLR} for the 1:30 AM/PM average of the same seven day period.

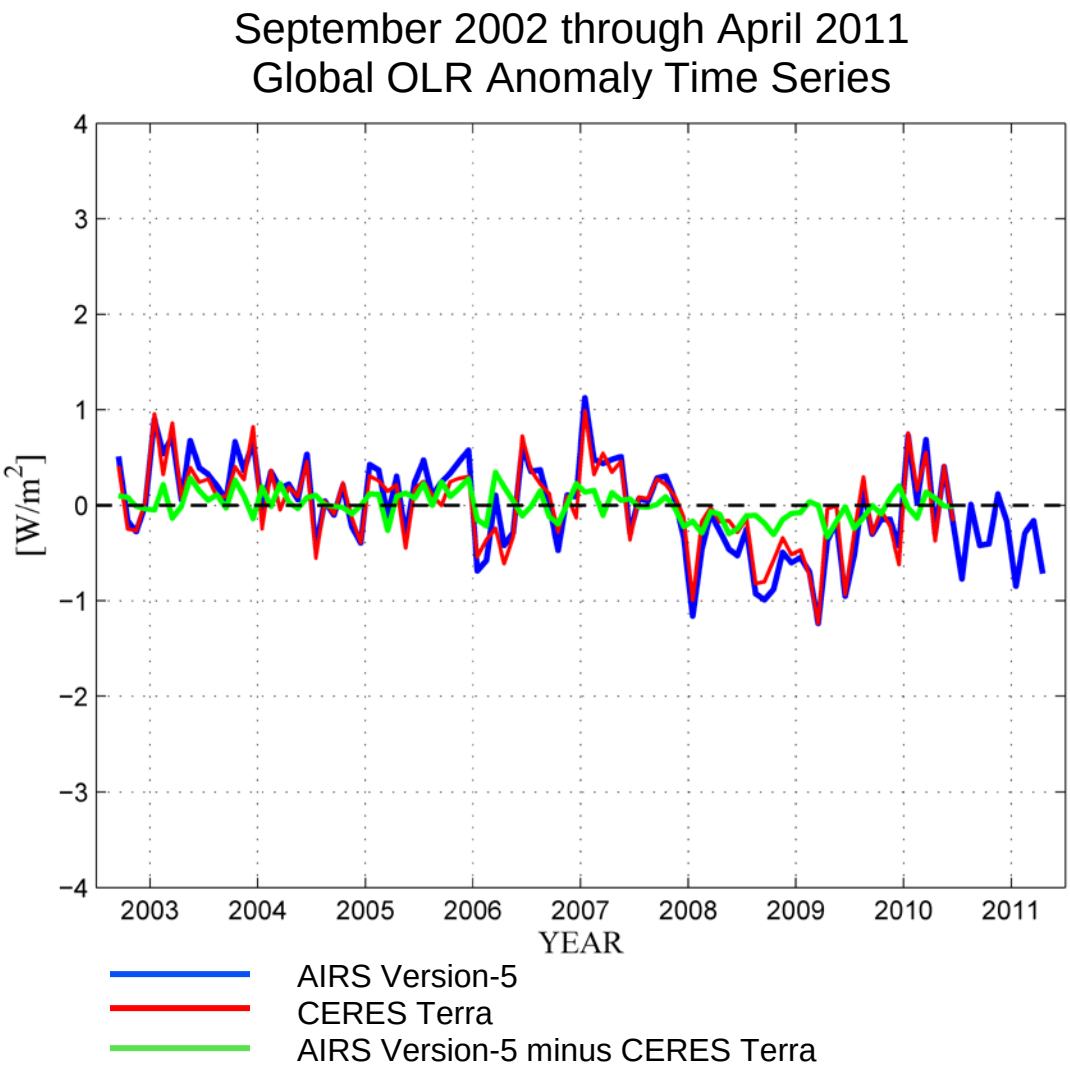

Figure 4a. Global mean AIRS and CERES Terra monthly mean OLR anomaly time series and their anomaly differences for the overlap period September 2002 through June 2010.

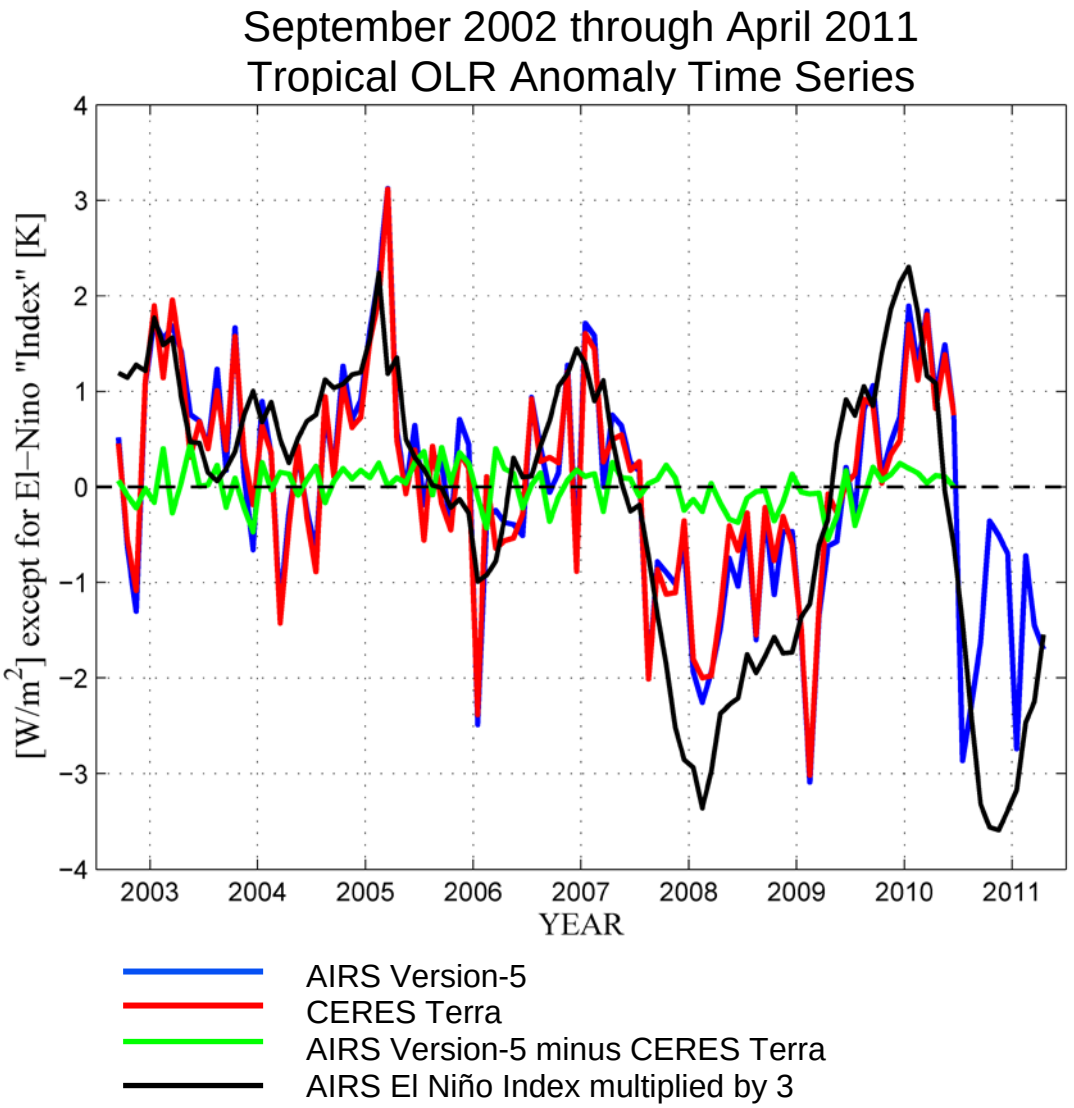

Figure 4b. Tropical (20°N to 20°S) mean monthly mean OLR anomaly time series and anomaly differences of AIRS and CERES Terra for the overlap period September 2002 through June 2010. Also shown in black is the AIRS El Niño index multiplied by 3.

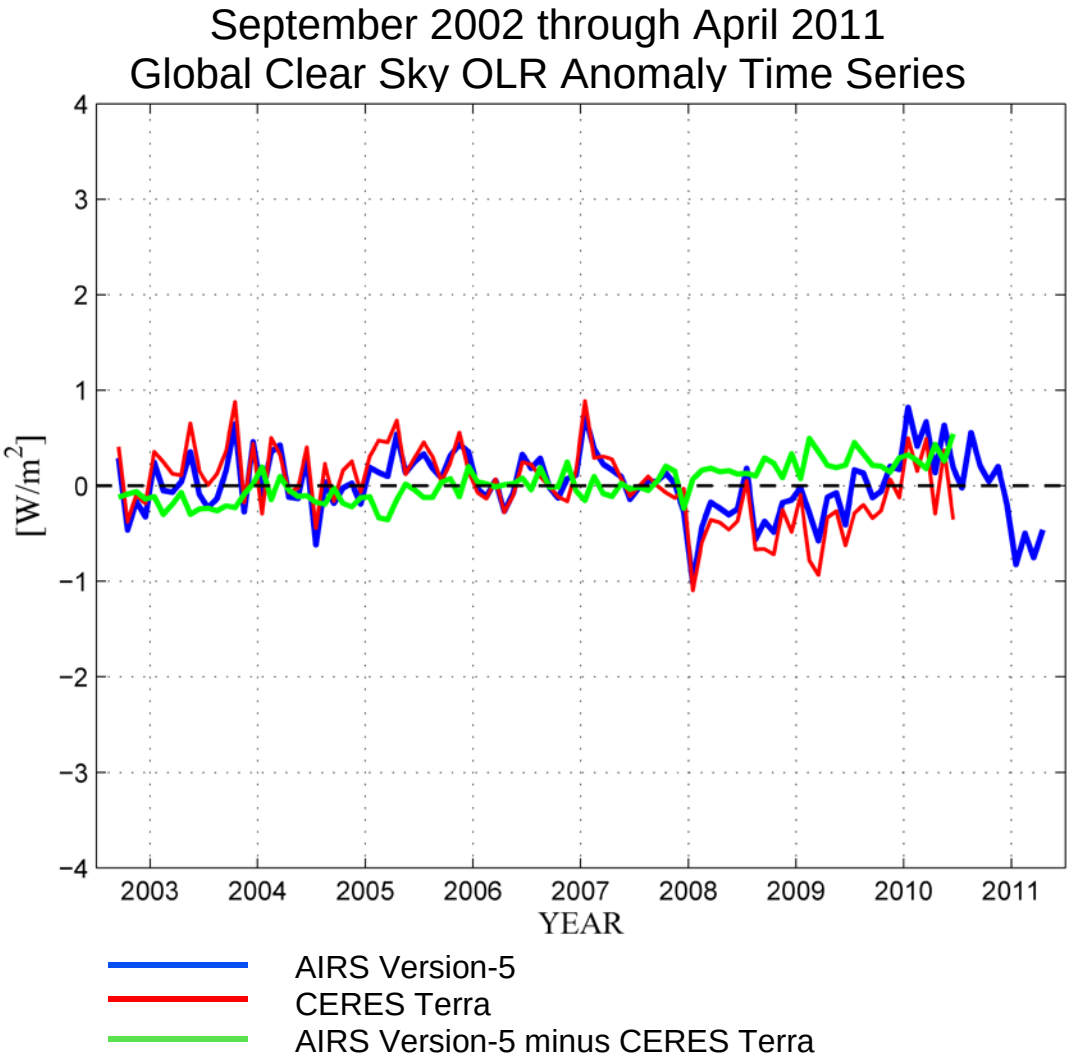

Figure 5a. Global mean monthly mean OLR_{CLR} anomaly time series and anomaly differences of AIRS and CERES Terra for the overlap period September 2002 through June 2010.

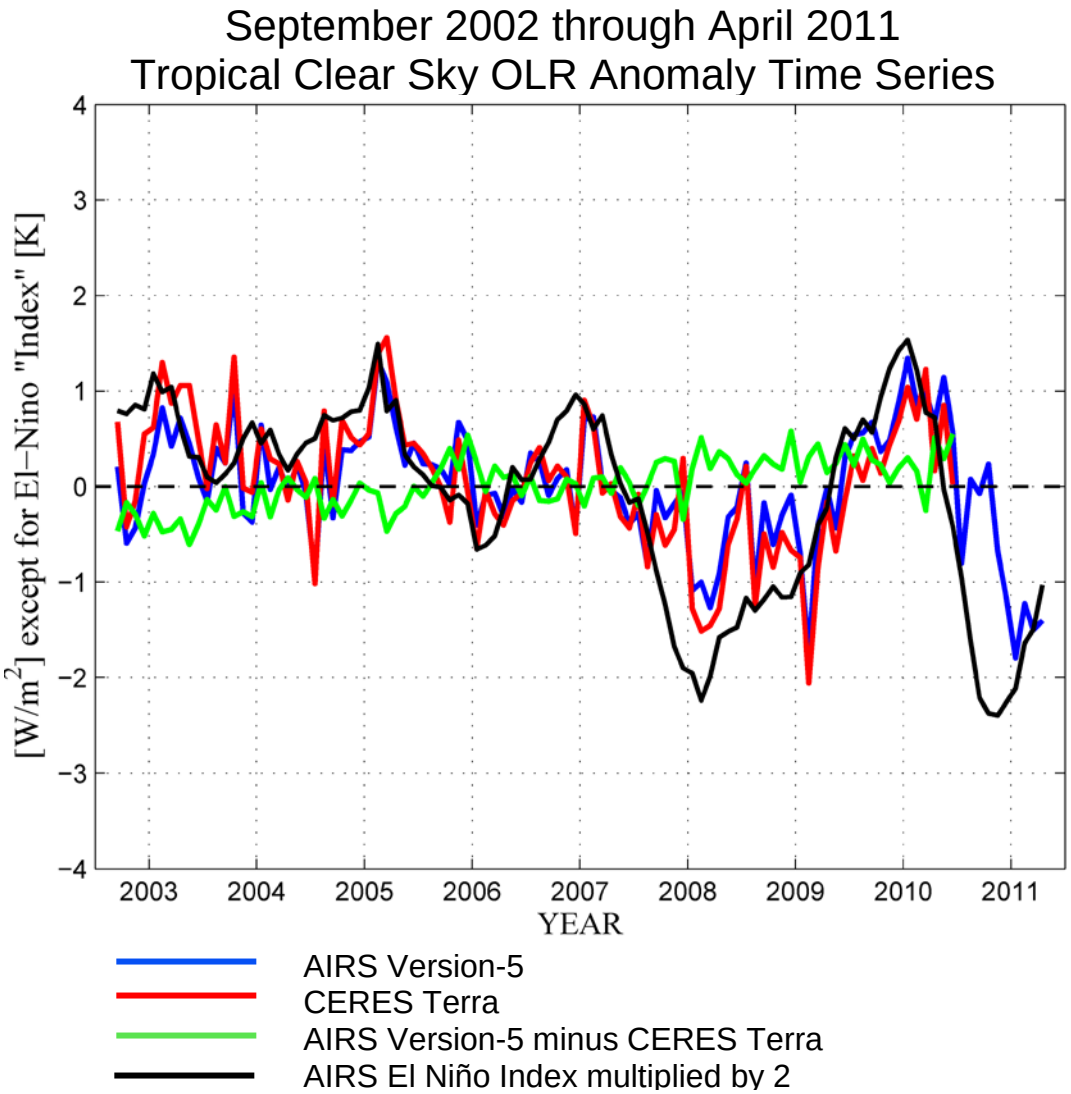

Figure 5b. Tropical (20°N to 20°S) mean monthly mean OLR_{CLR} anomaly time series and anomaly differences of AIRS and CERES Terra for the overlap period September 2002 through June 2010. Also shown in black is the AIRS El Niño index multiplied by 2.

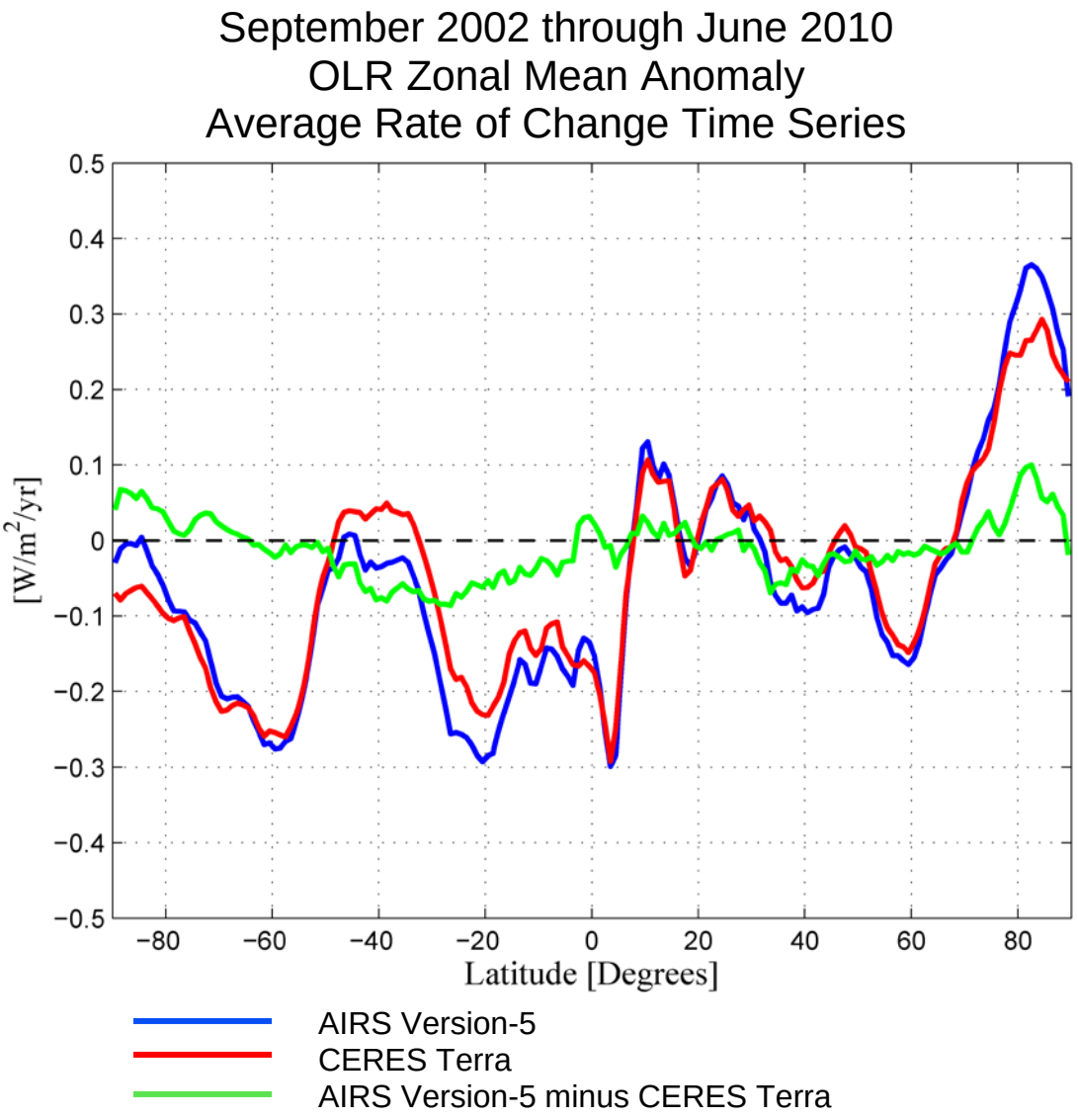

Figure 6a. Zonal mean Average Rates of Change (ARC's) for AIRS and CERES Terra OLR monthly mean time series for the period September 2002 through June 2010, as well as the difference of the two sets of ARC's. The majority of the decrease in global OLR during this period originates in the tropics south of 8°N.

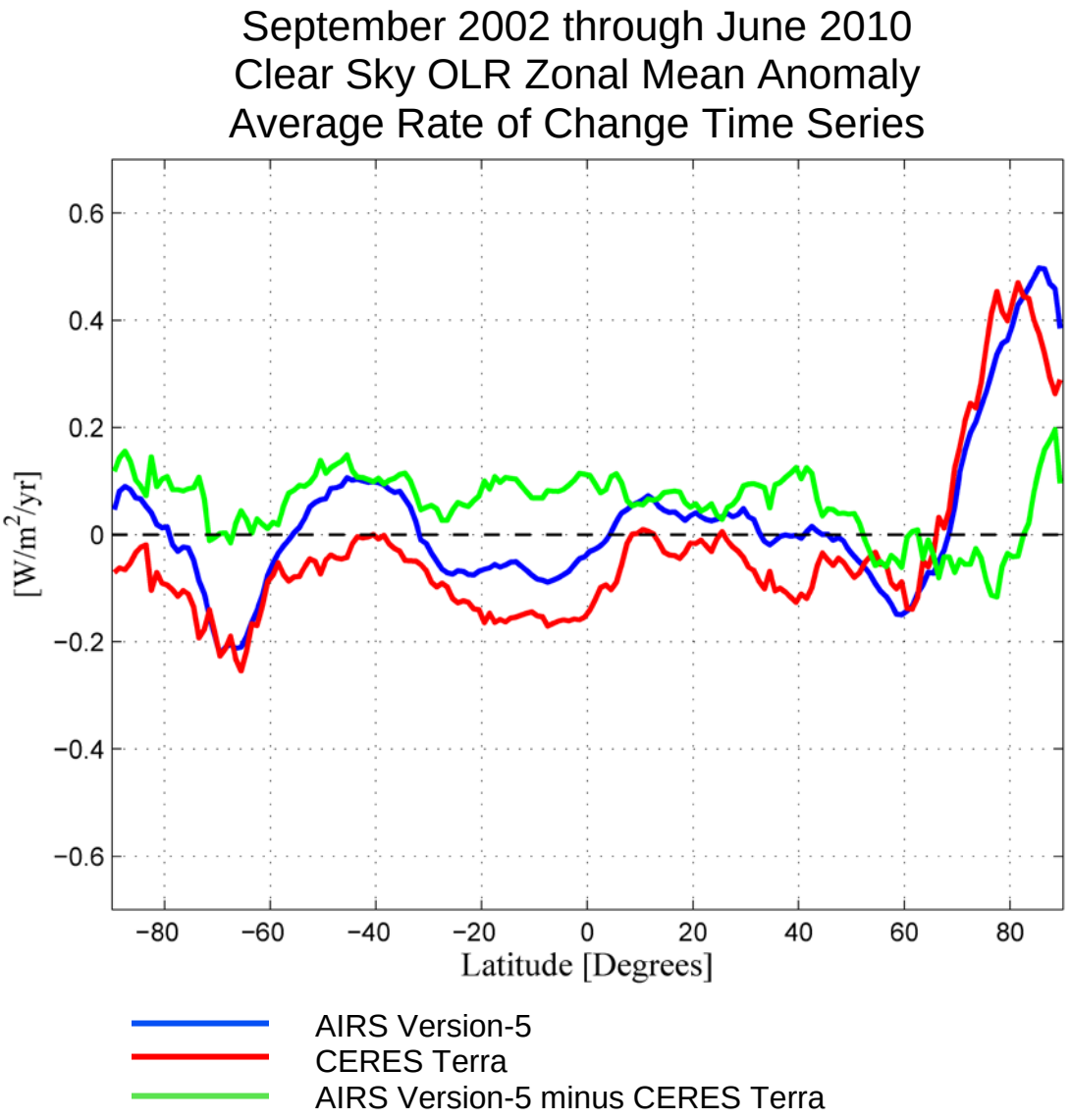

Figure 6b. Zonal mean ARC's for AIRS and CERES Terra OLR_{CLR} monthly mean time series for the period September 2002 through June 2010, as well as the difference of the two sets of ARC's.

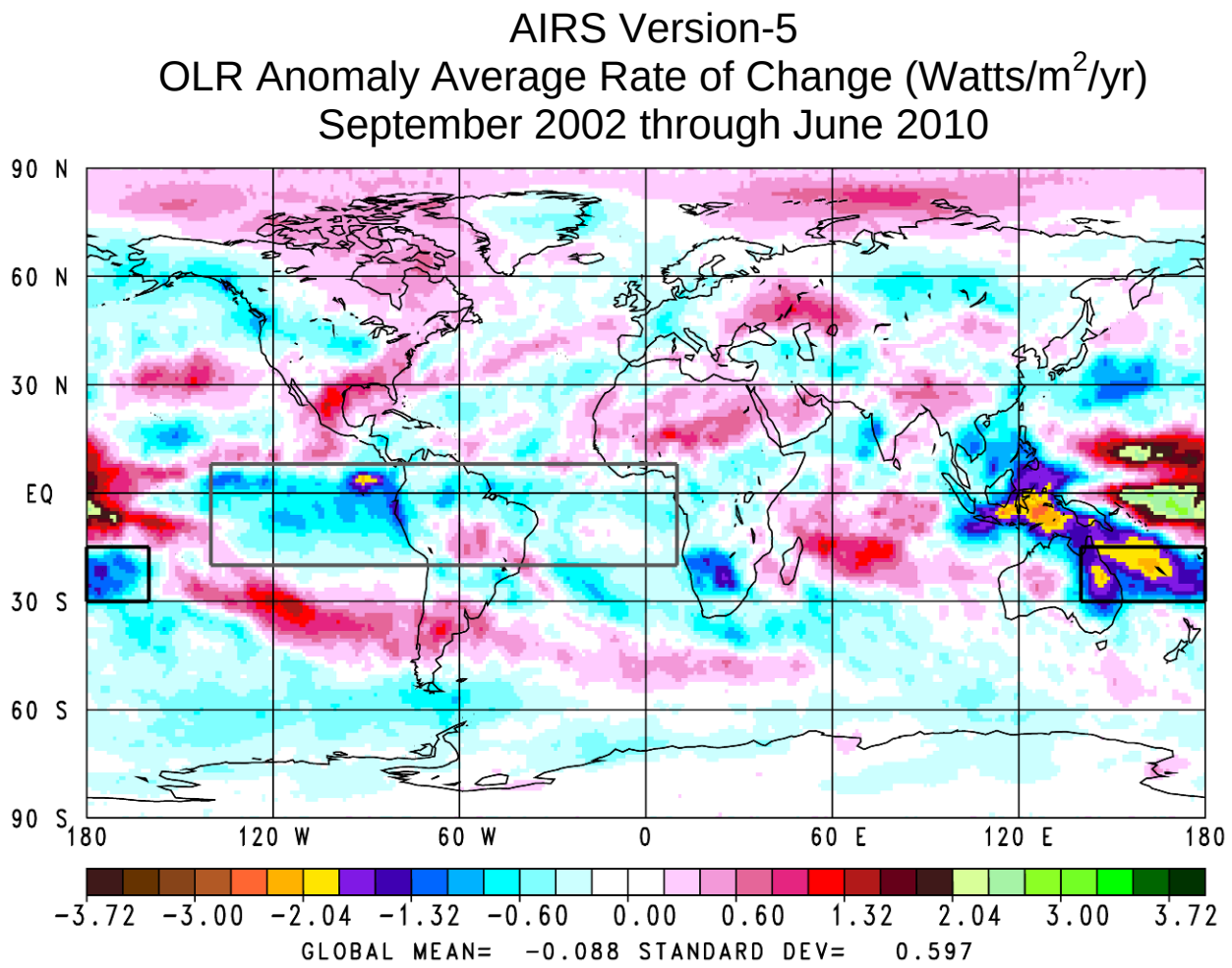

Figure 7a. Spatial 1° latitude by 1° longitude distribution of global AIRS OLR ARC's over the time period September 2002 through June 2010. OLR Region 1 is outlined in gray and OLR Region 2 is outlined in black in this and most subsequent figures showing spatial distributions of ARC's of different parameters.

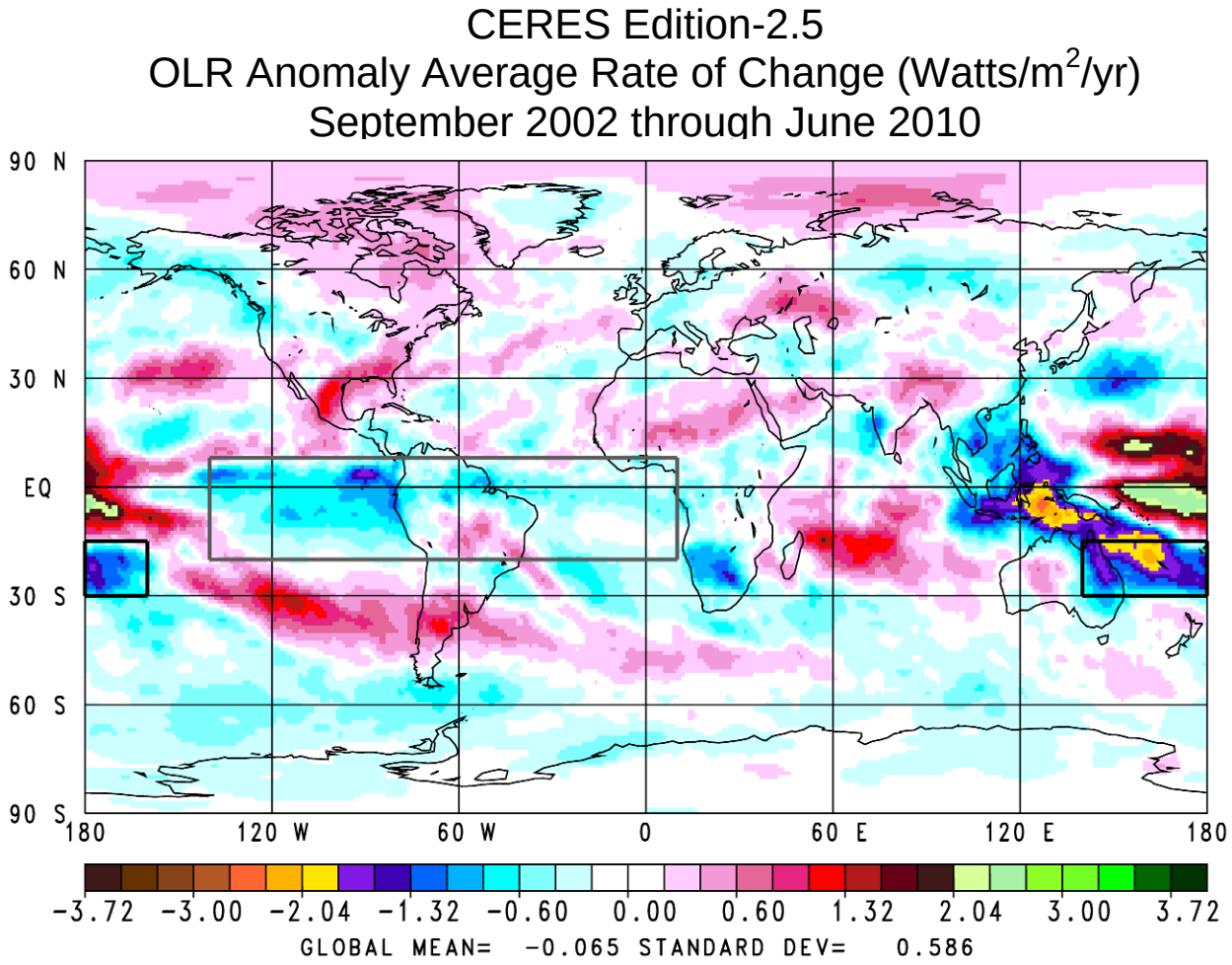

Figure 7b. Spatial 1° latitude by 1° longitude distribution of global CERES OLR ARC's over the time period September 2002 through June 2010.

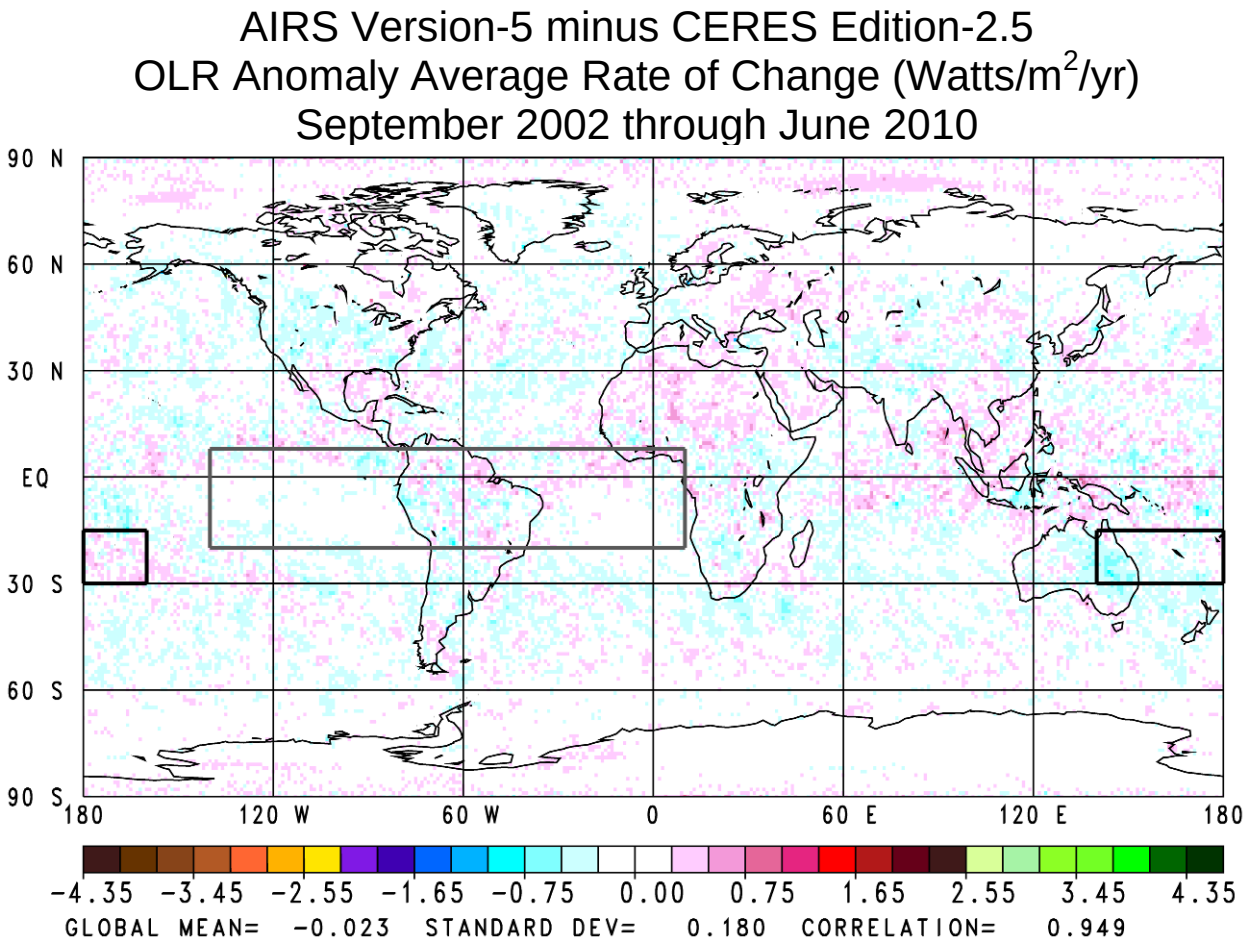

Figure 7c. Spatial distribution of ARC's of AIRS minus CERES OLR.

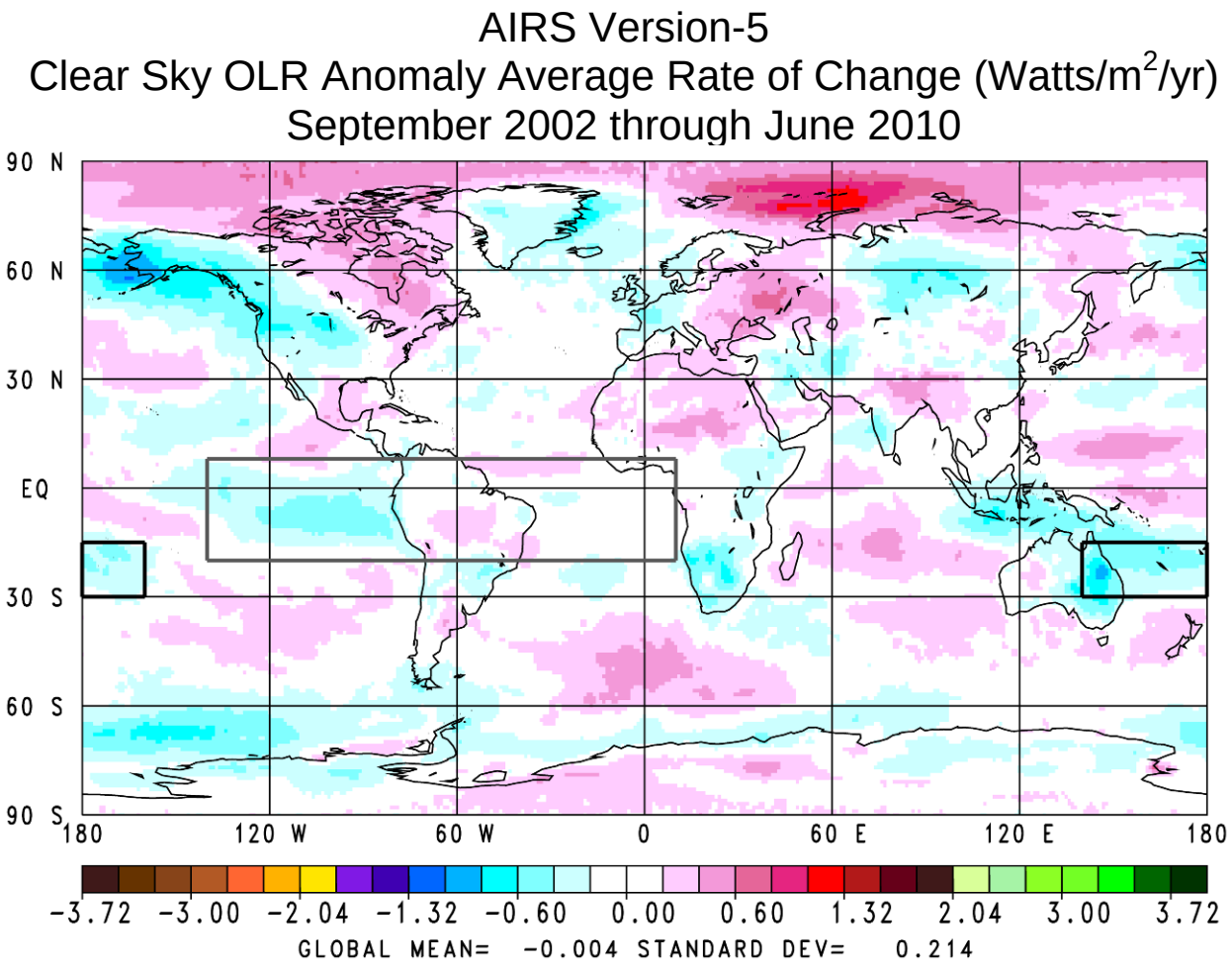

Figure 8a. Spatial 1° latitude by 1° longitude distribution of global AIRS OLR_{CLR} ARC's over the time period September 2002 through June 2010.

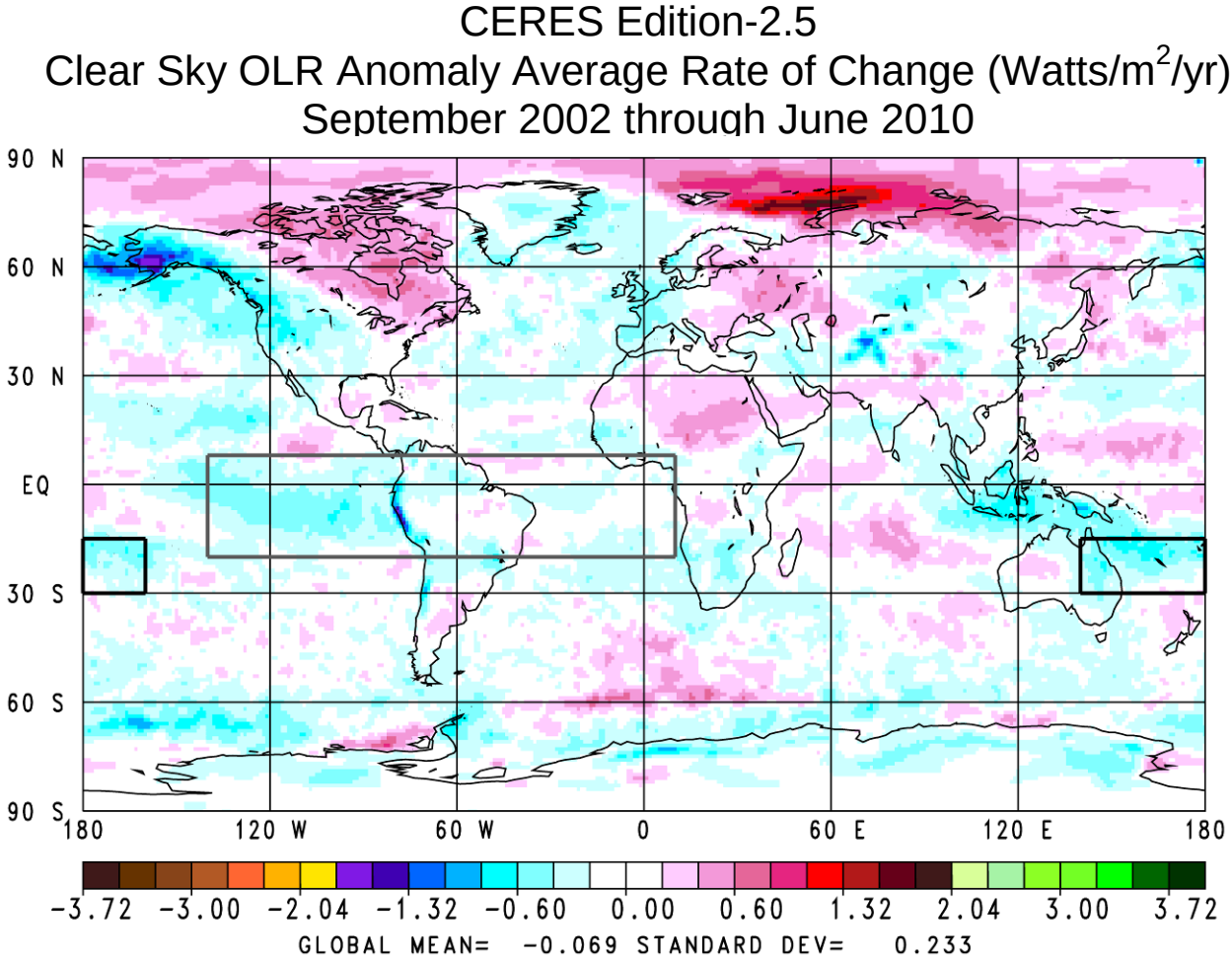

Figure 8b. Spatial 1° latitude by 1° longitude distribution of global CERES OLR_{CLR} ARC's over the time period September 2002 through June 2010.

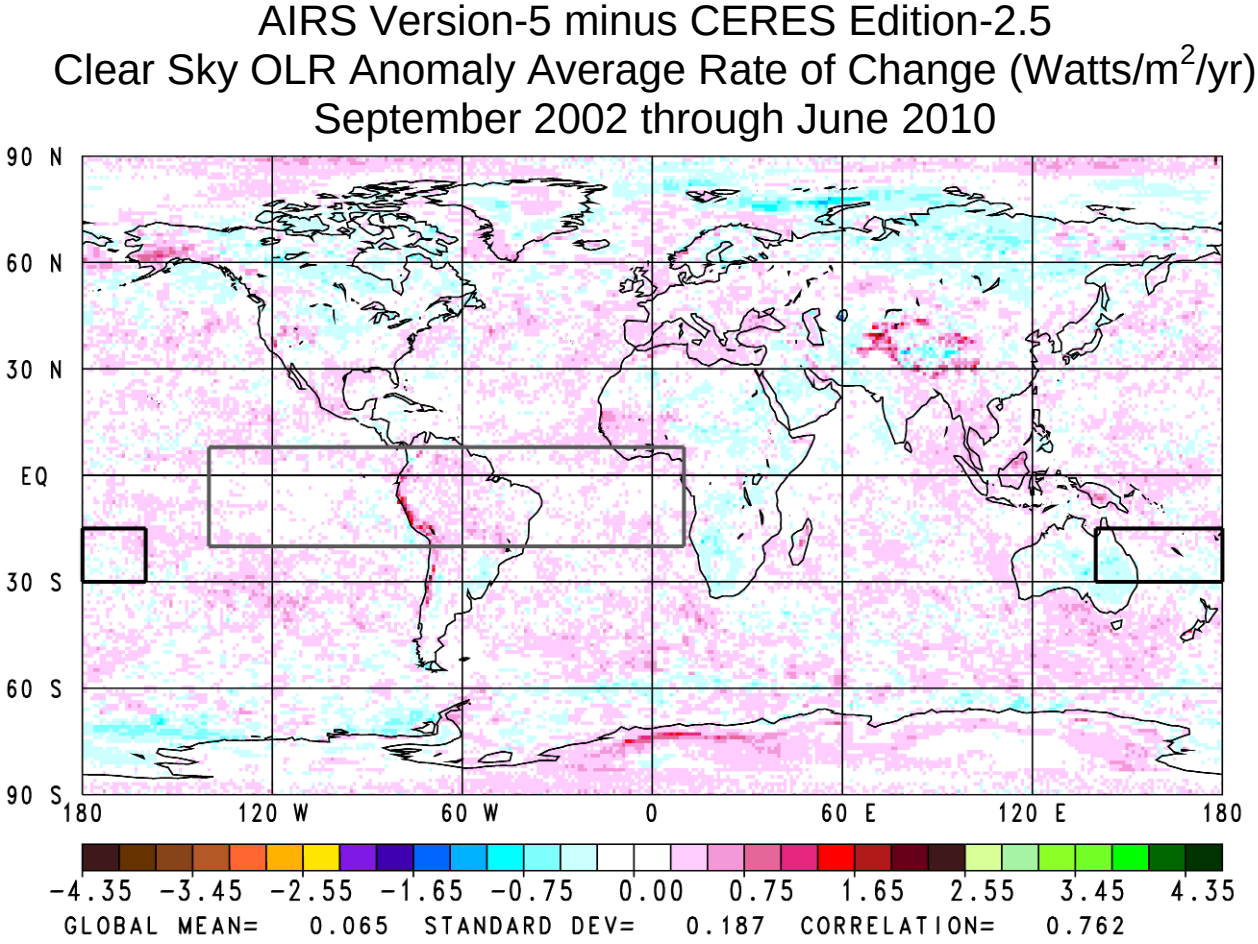

Figure 8c. Spatial distribution of ARC's of AIRS minus CERES OLR_{CLR}.

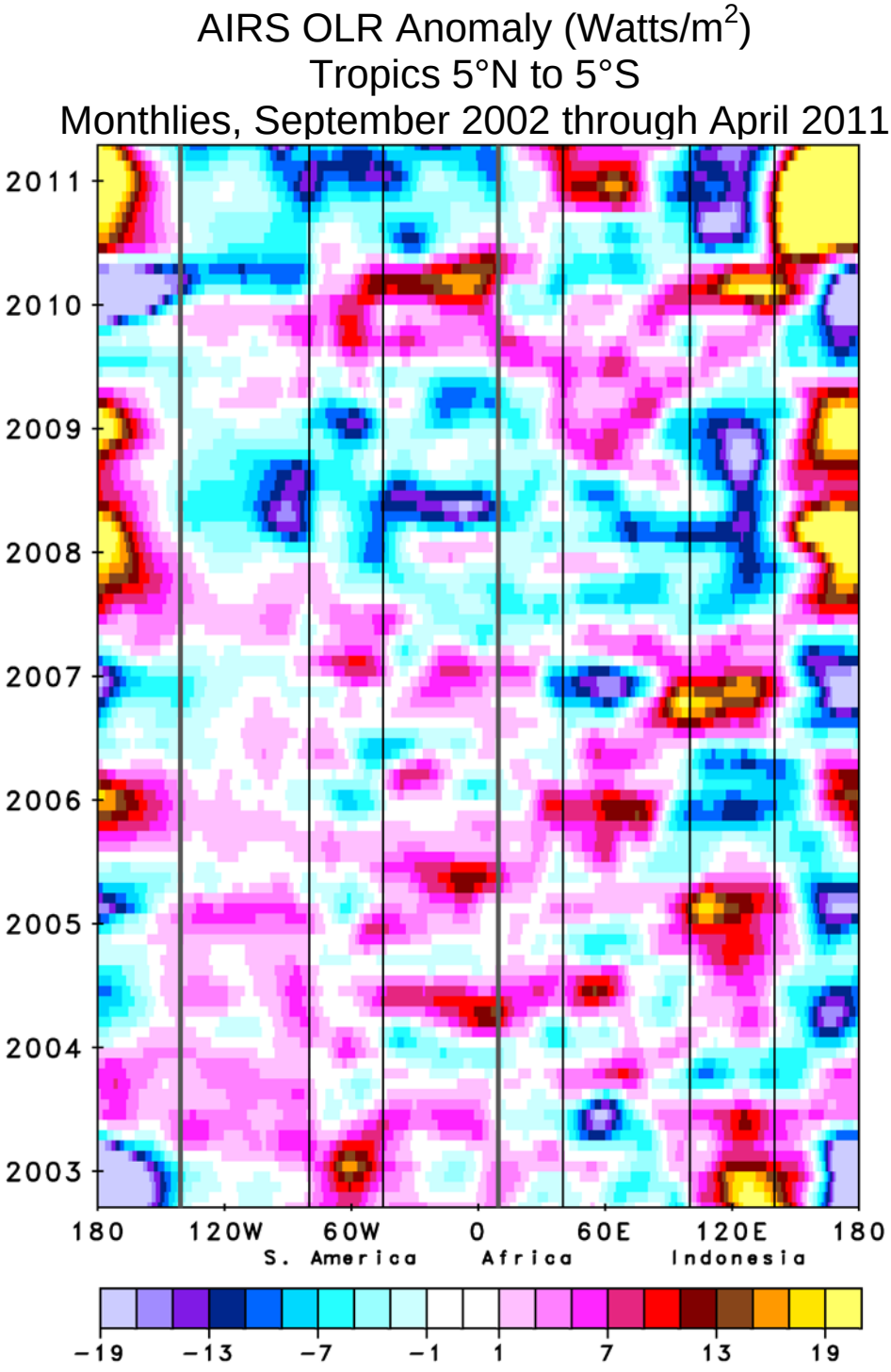

Figure 9a. Hovmöller diagram for time series of monthly mean AIRS OLR anomalies integrated over the latitude range 5°N through 5°S in each 1° longitude bin for the period September 2002 through April 2011. The longitudinal domain of OLR Region 1 is indicated by the gray vertical lines in this and most subsequent Hovmöller diagrams.

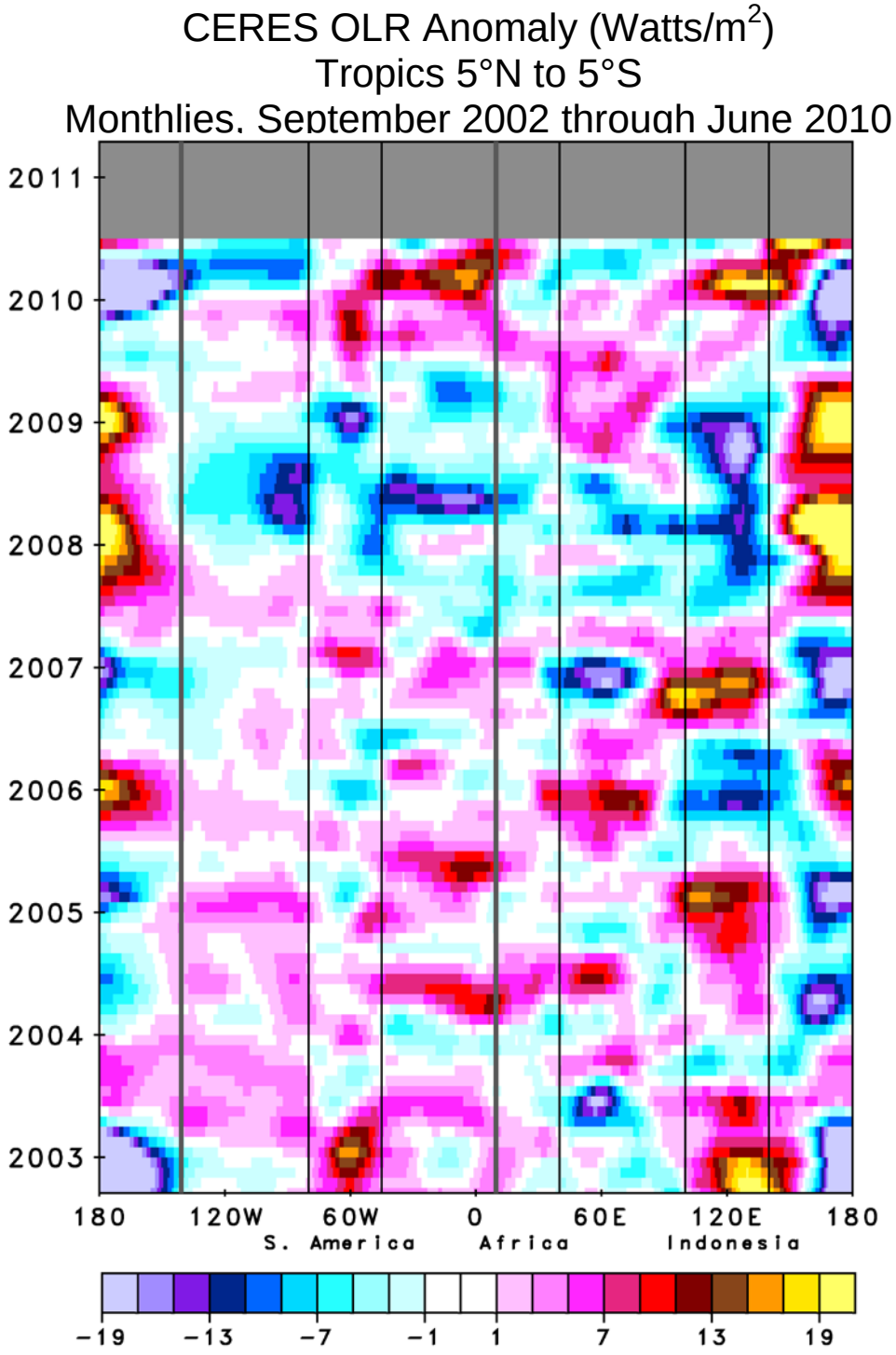

Figure 9b. Hovmöller diagram for time series of monthly mean CERES OLR anomalies integrated over the latitude range 5°N through 5°S in each 1° longitude bin for the period September 2002 through June 2010.

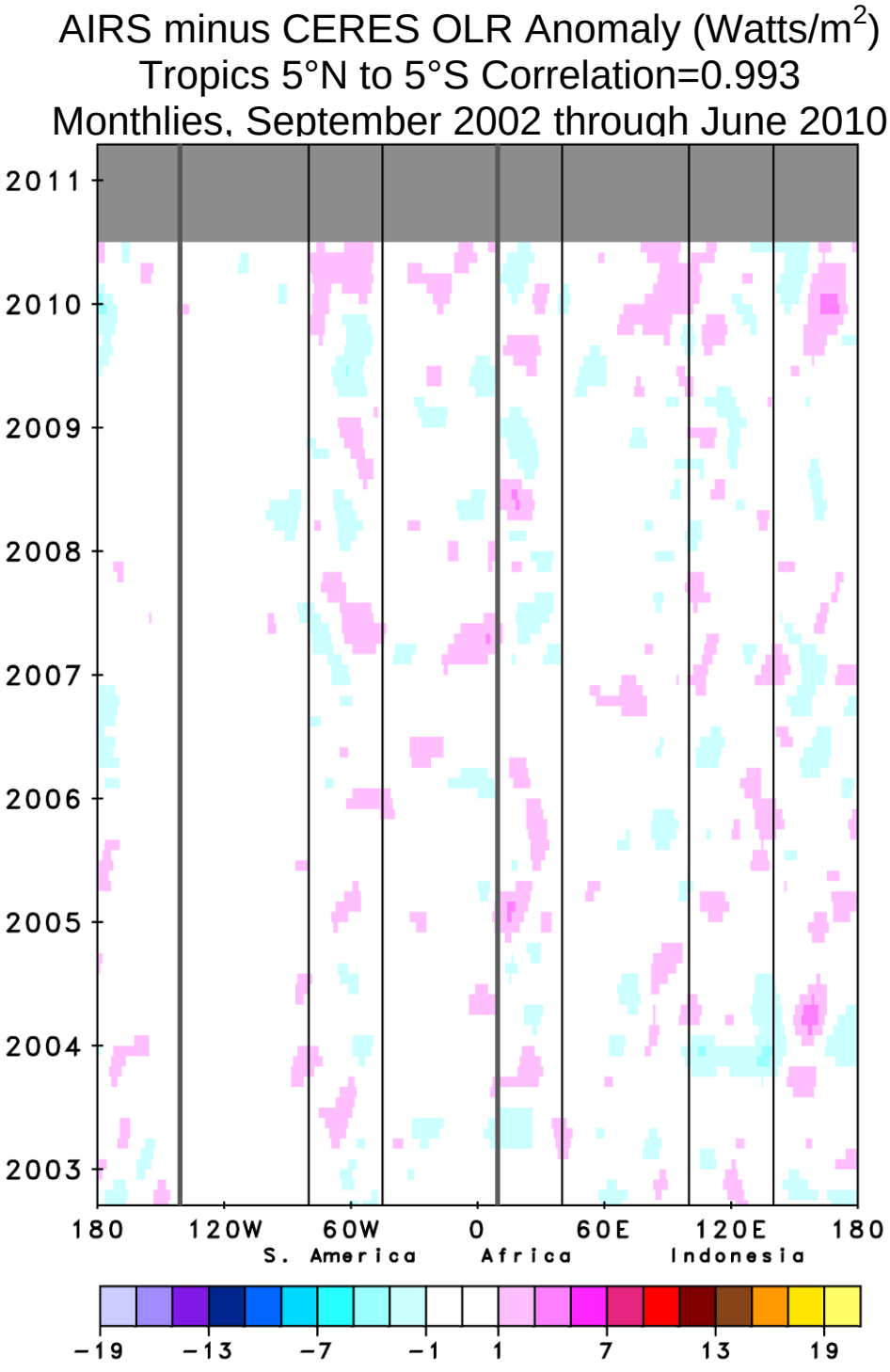

Figure 9c. Hovmöller diagram for the difference between AIRS OLR and CERES OLR.

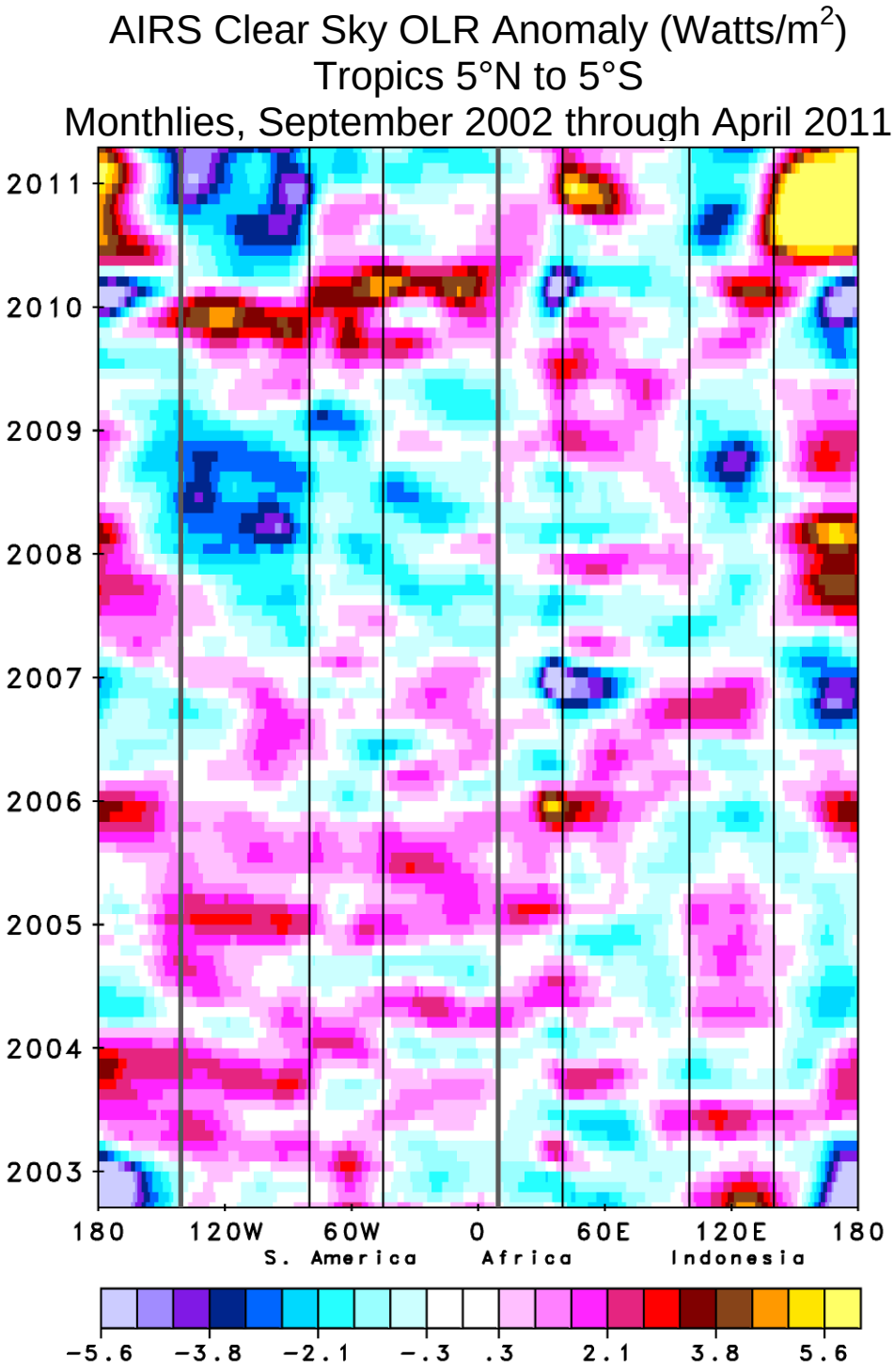

Figure 10a. Hovmöller diagram for time series of monthly mean AIRS OLR_{CLR} anomalies integrated over the latitude range 5°N through 5°S in each 1° longitude bin for the period September 2002 through April 2011.

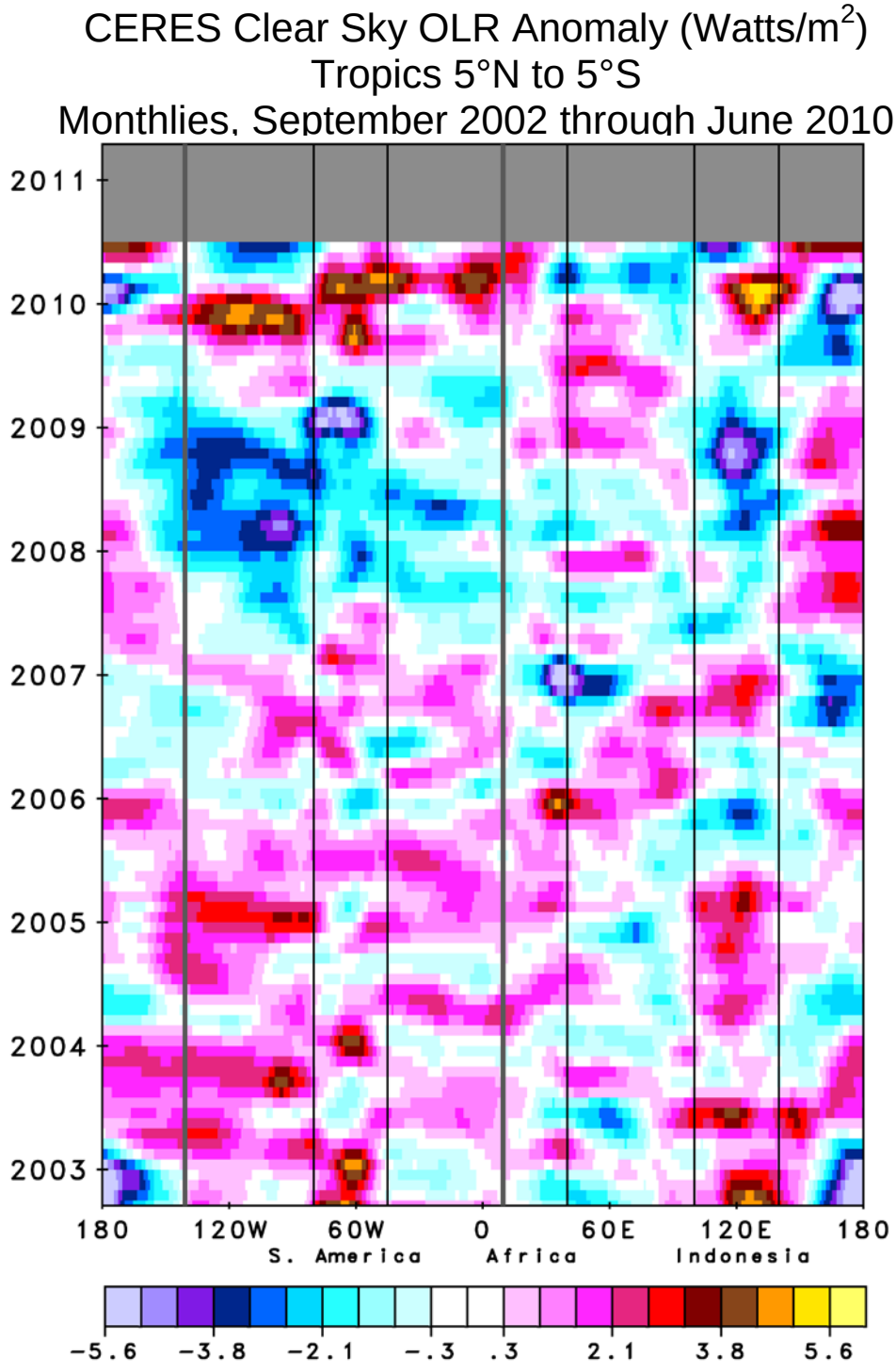

Figure 10b. Hovmöller diagram for time series of monthly mean CERES OLR_{CLR} anomalies integrated over the latitude range 5°N through 5°S in each 1° longitude bin for the period September 2002 through June 2010.

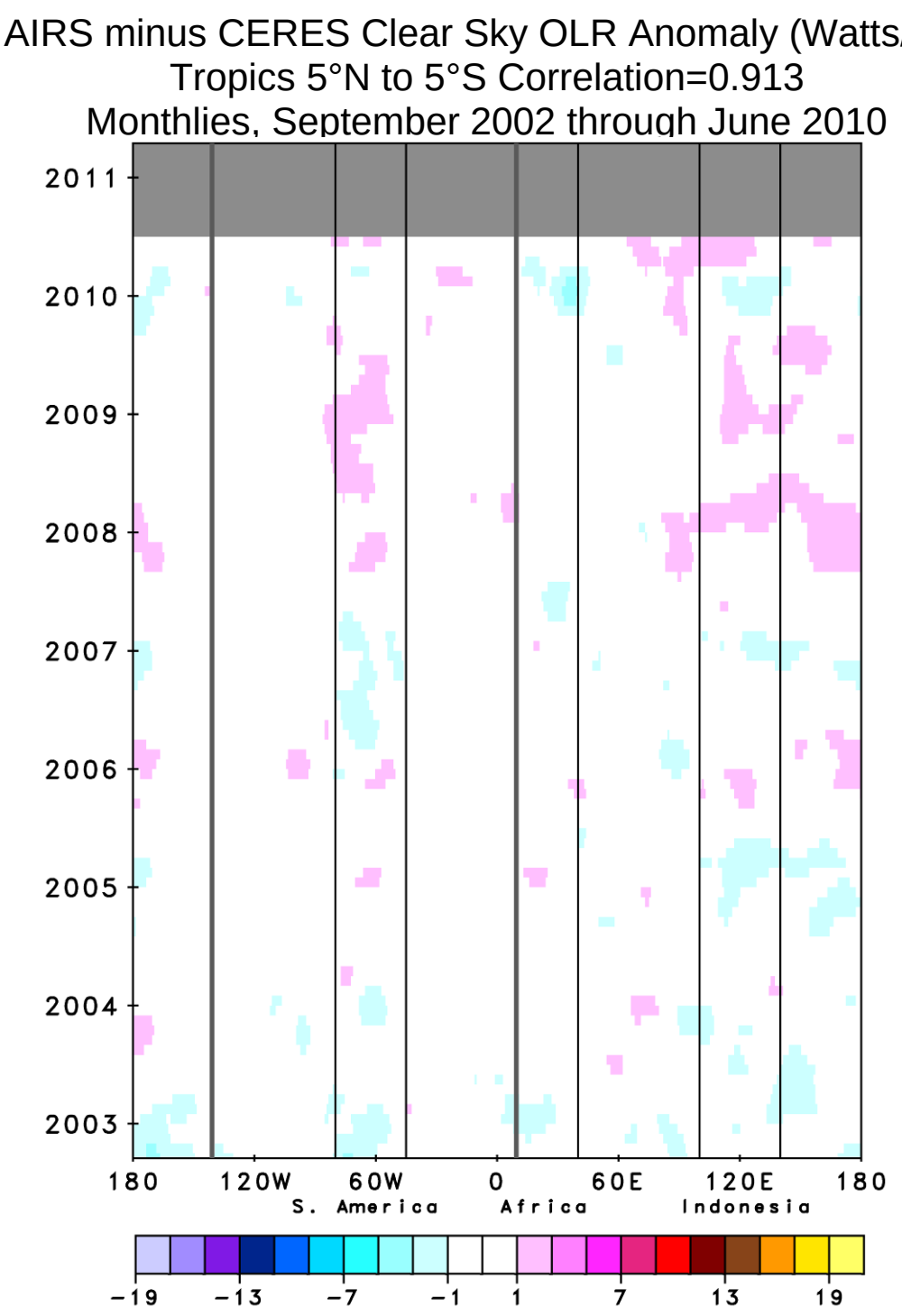

Figure 10c. Hovmöller diagram for the difference between AIRS OLR and CERES OLR_{CLR}

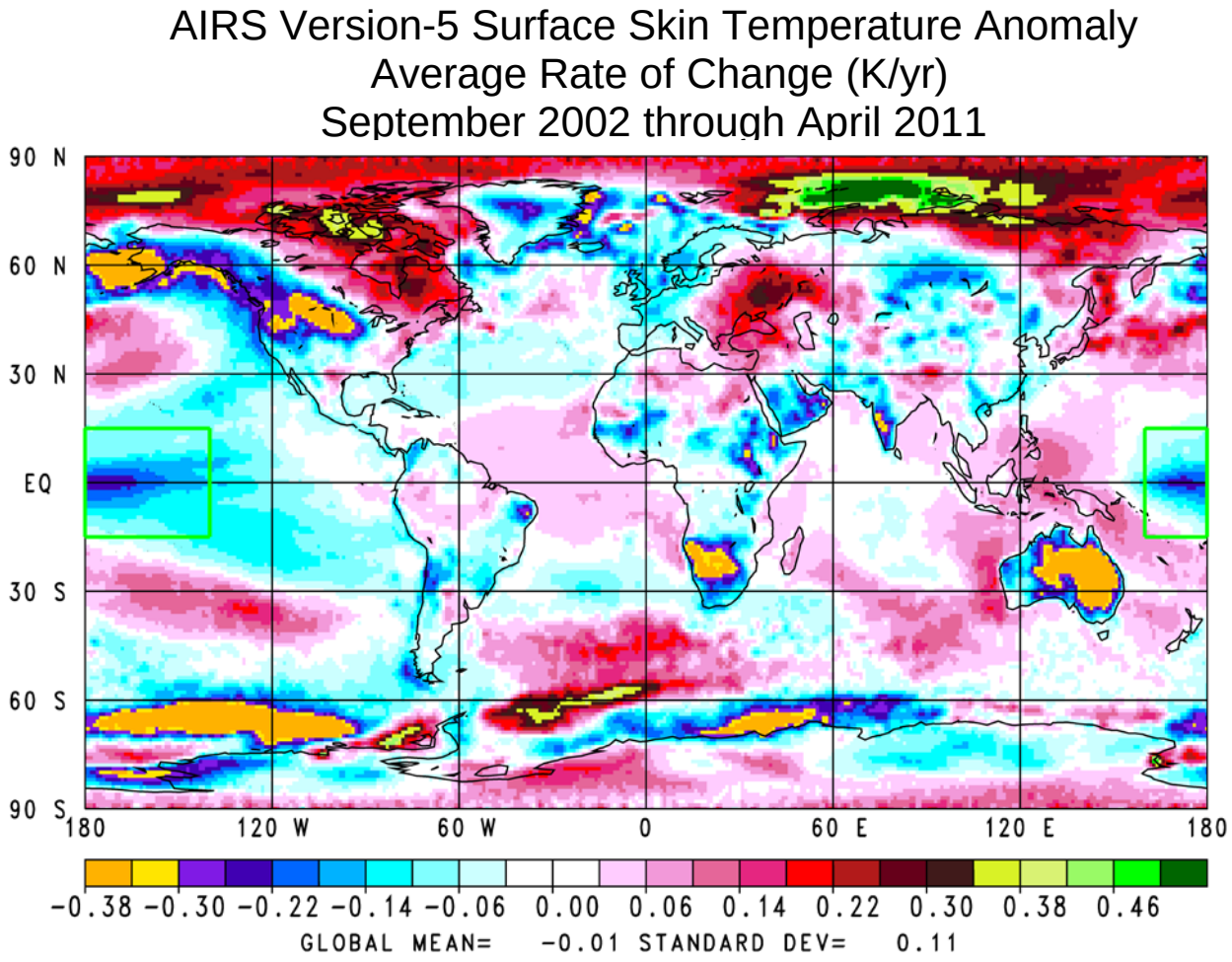

Figure 11a. Spatial distribution of Average Rate of Change of AIRS surface skin temperature (K/yr) over the period September 2002 through April 2011. The spatial domain of the AIRS El Niño region is outlined in green.

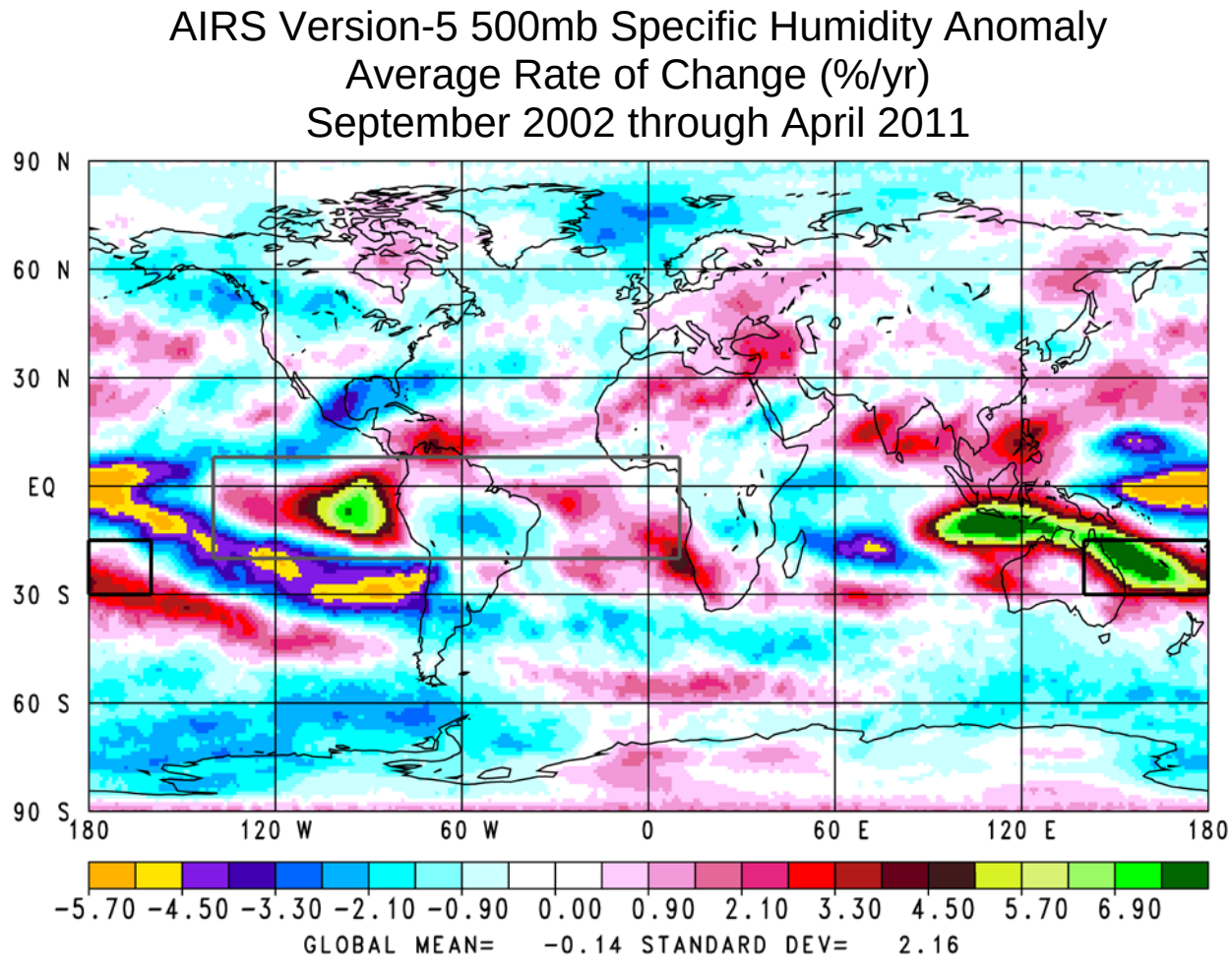

Figure 11b. Spatial distribution of Average Rate of Change of AIRS 500 mb specific humidity (%/yr) over the period September 2002 through April 2011.

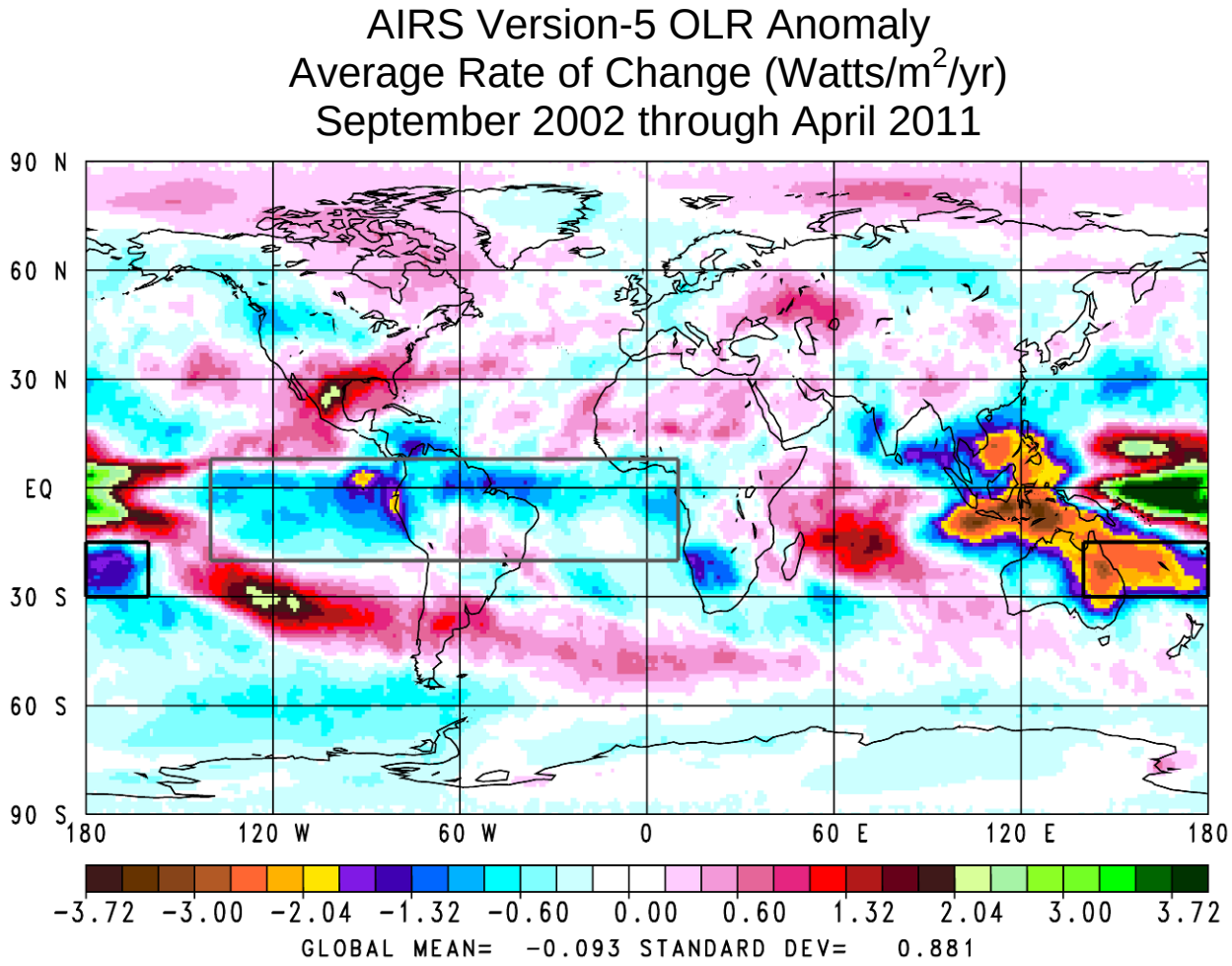

Figure 11c. Spatial distribution of Average Rate of Change of AIRS OLR (W/m^2/yr) over the period September 2002 through April 2011.

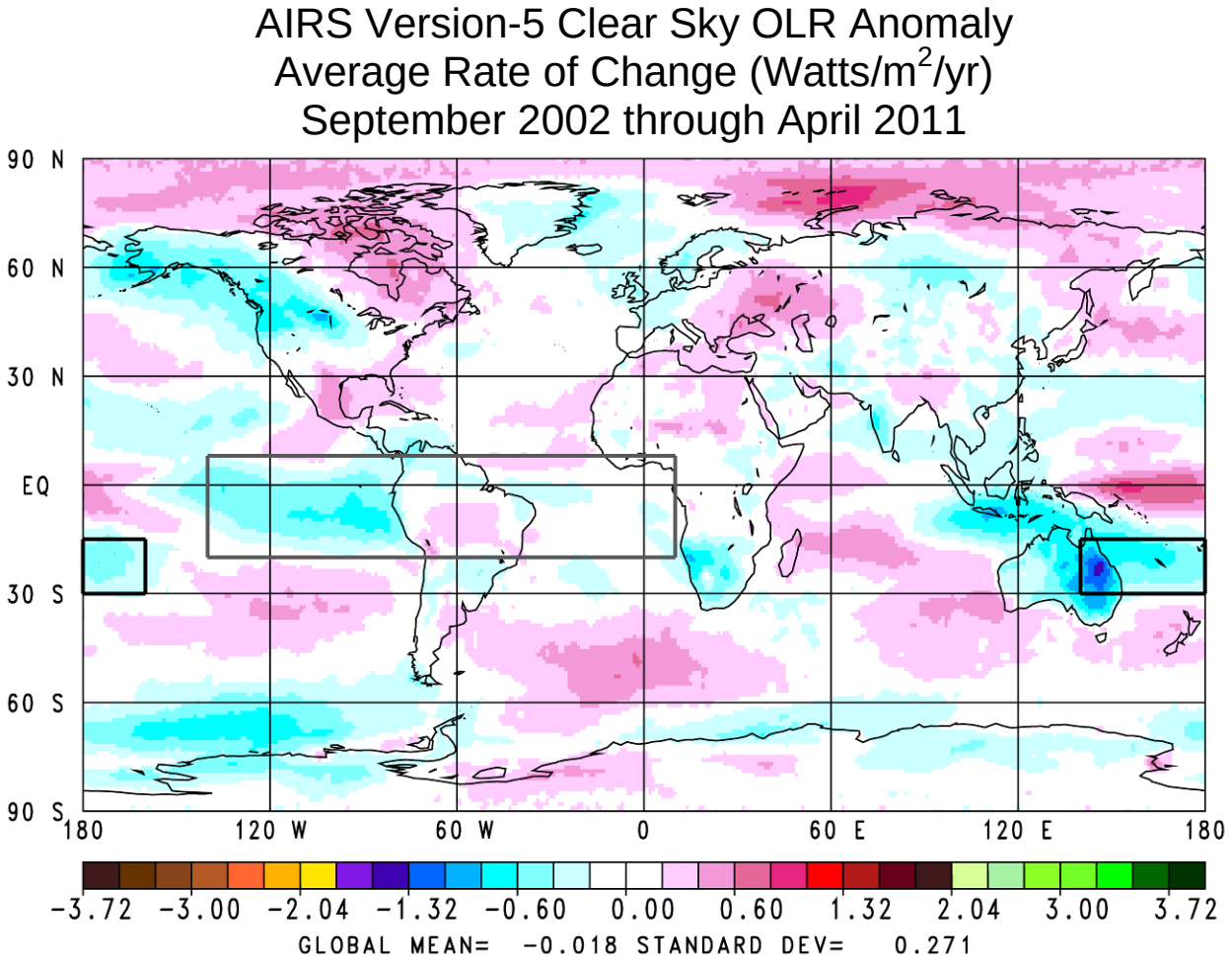

Figure 11d. Spatial distribution of Average Rate of Change of AIRS Clear Sky OLR ($W/m^2/yr$) over the period September 2002 through April 2011.

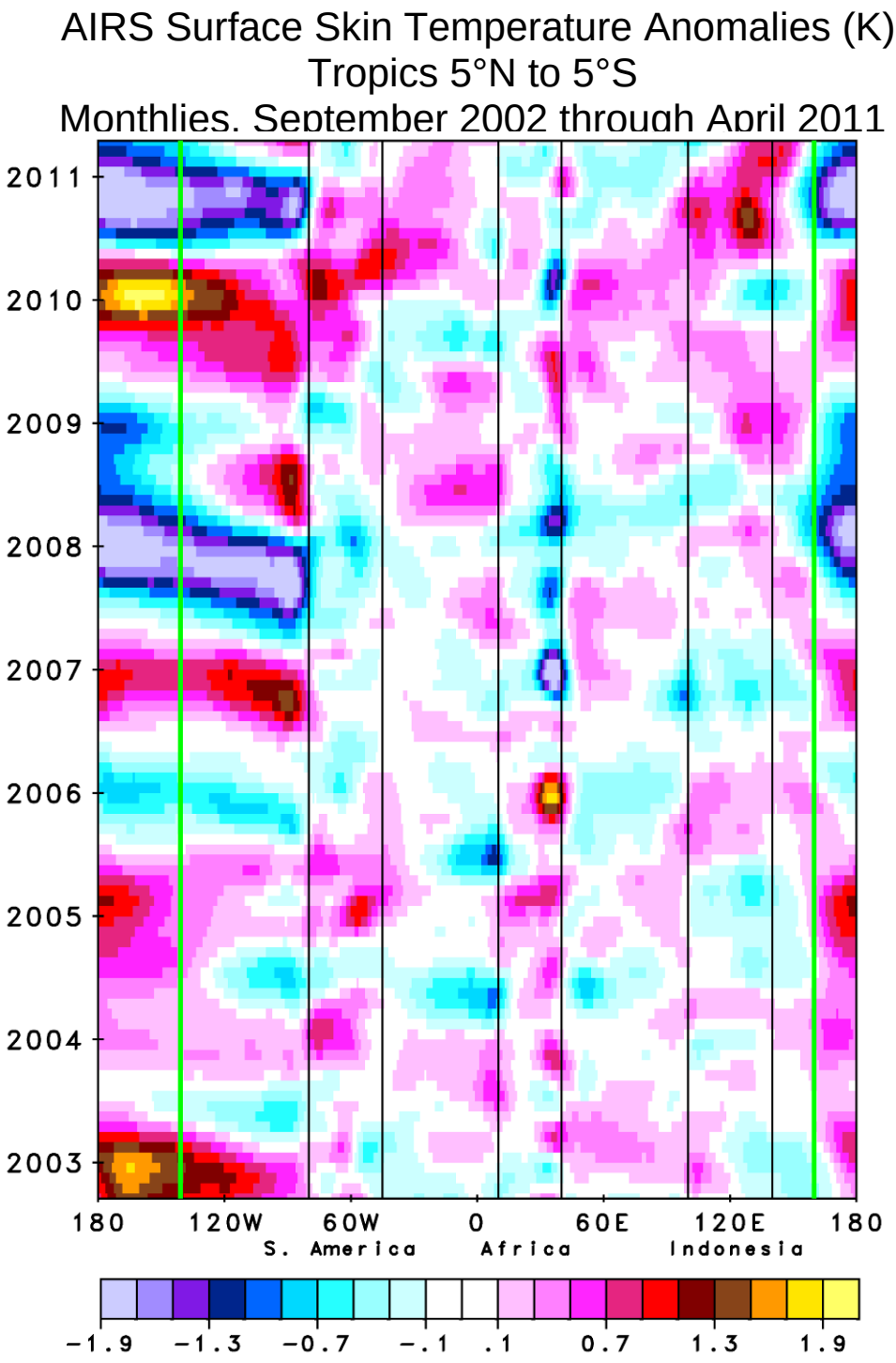

Figure 12a. Hovmöller diagram of AIRS Surface Skin Temperature anomalies (K). The longitudinal domain of the El Niño region is enclosed between the green vertical lines.

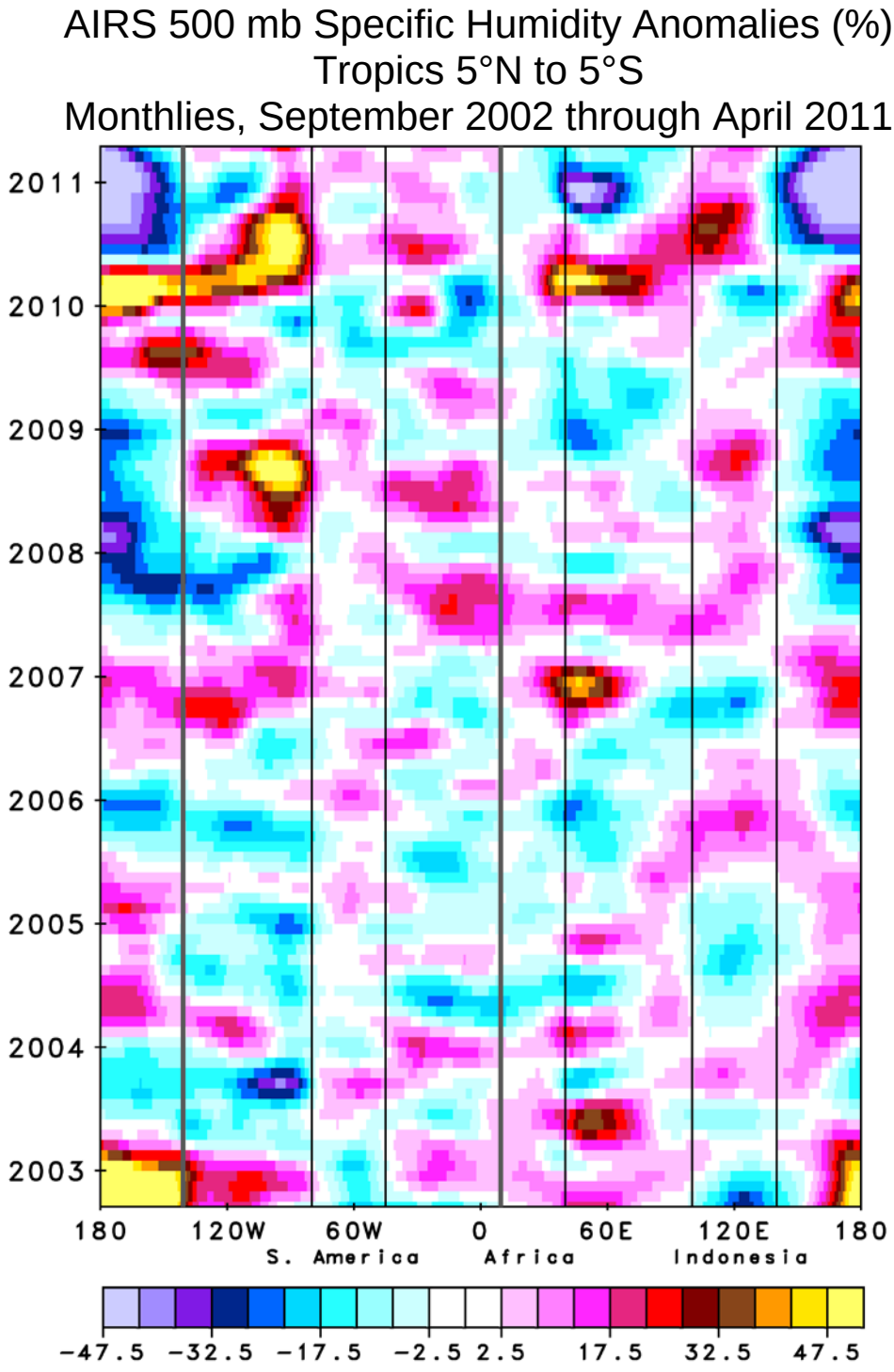

Figure 12b. Hovmöller diagram of AIRS 500 mb specific humidity anomalies (%). The longitudinal domain of Region 1 is enclosed between the gray vertical lines.

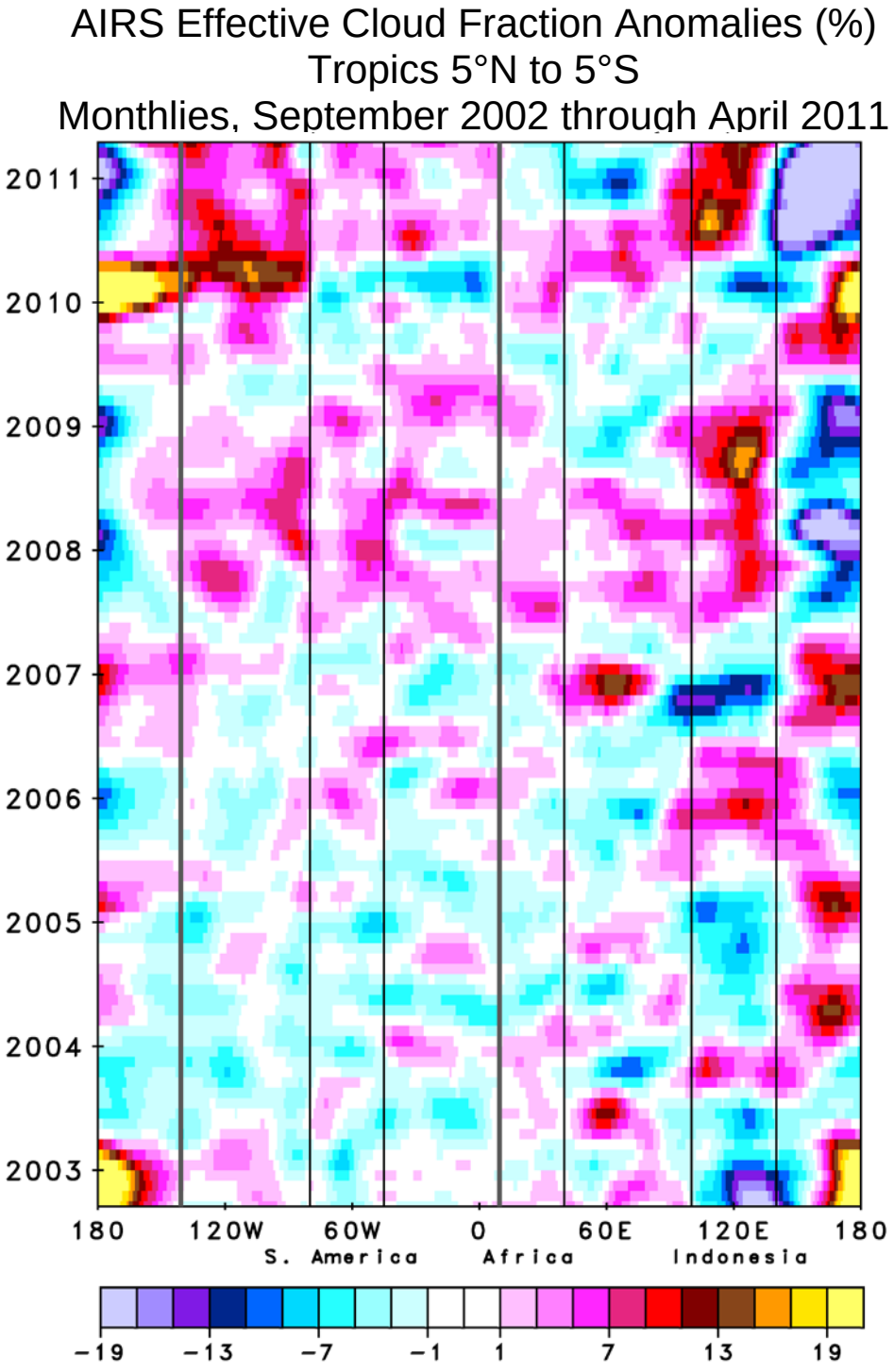

Figure 12c. Hovmöller diagram of AIRS effective cloud fraction anomalies (%). The longitudinal domain of Region 1 is enclosed between the gray vertical lines.

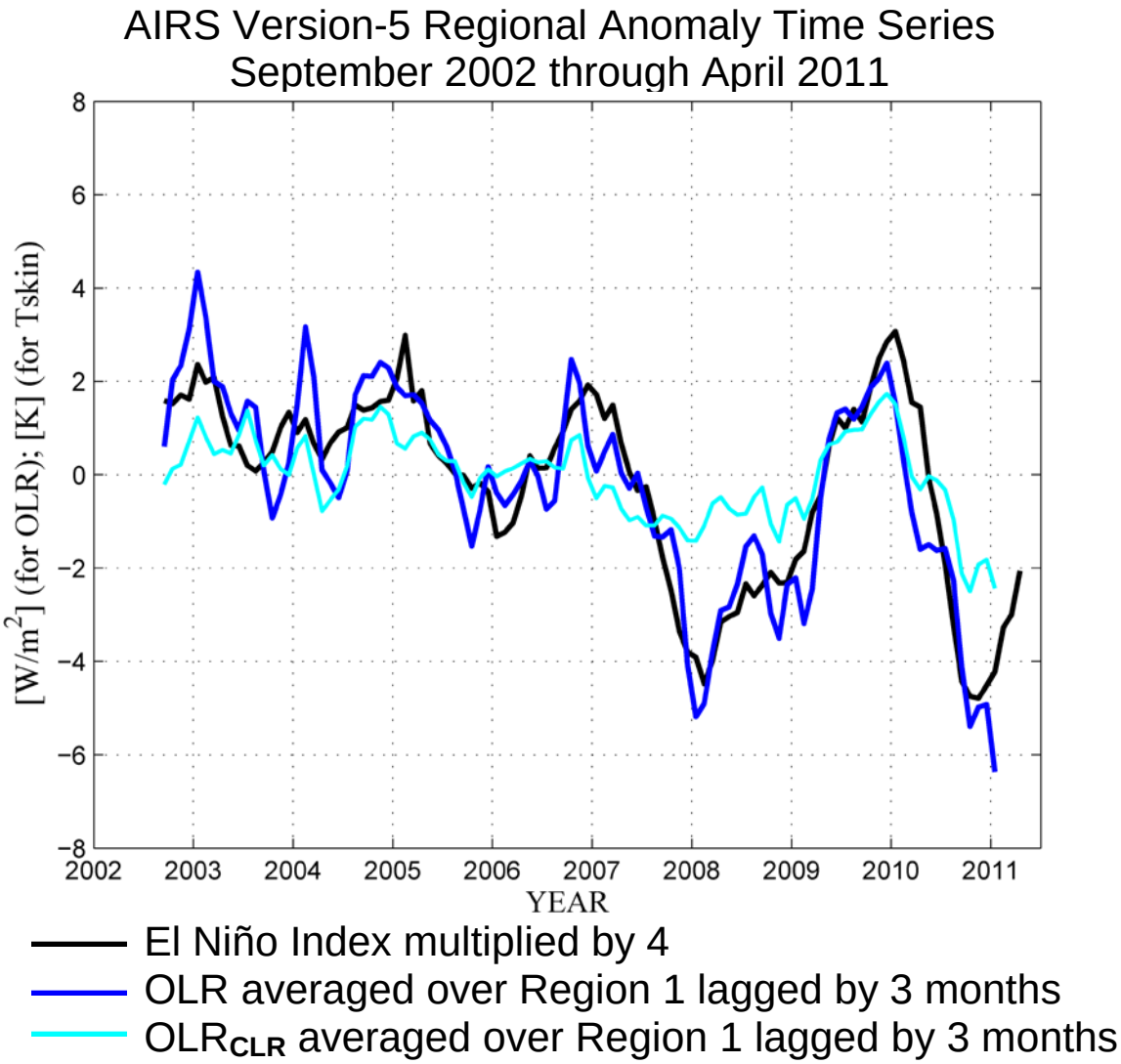

Figure 13a. AIRS OLR and OLR_{CLR} anomaly time series averaged over OLR Region 1 superimposed on the AIRS El Niño index multiplied by 4 and plotted 3 months earlier.

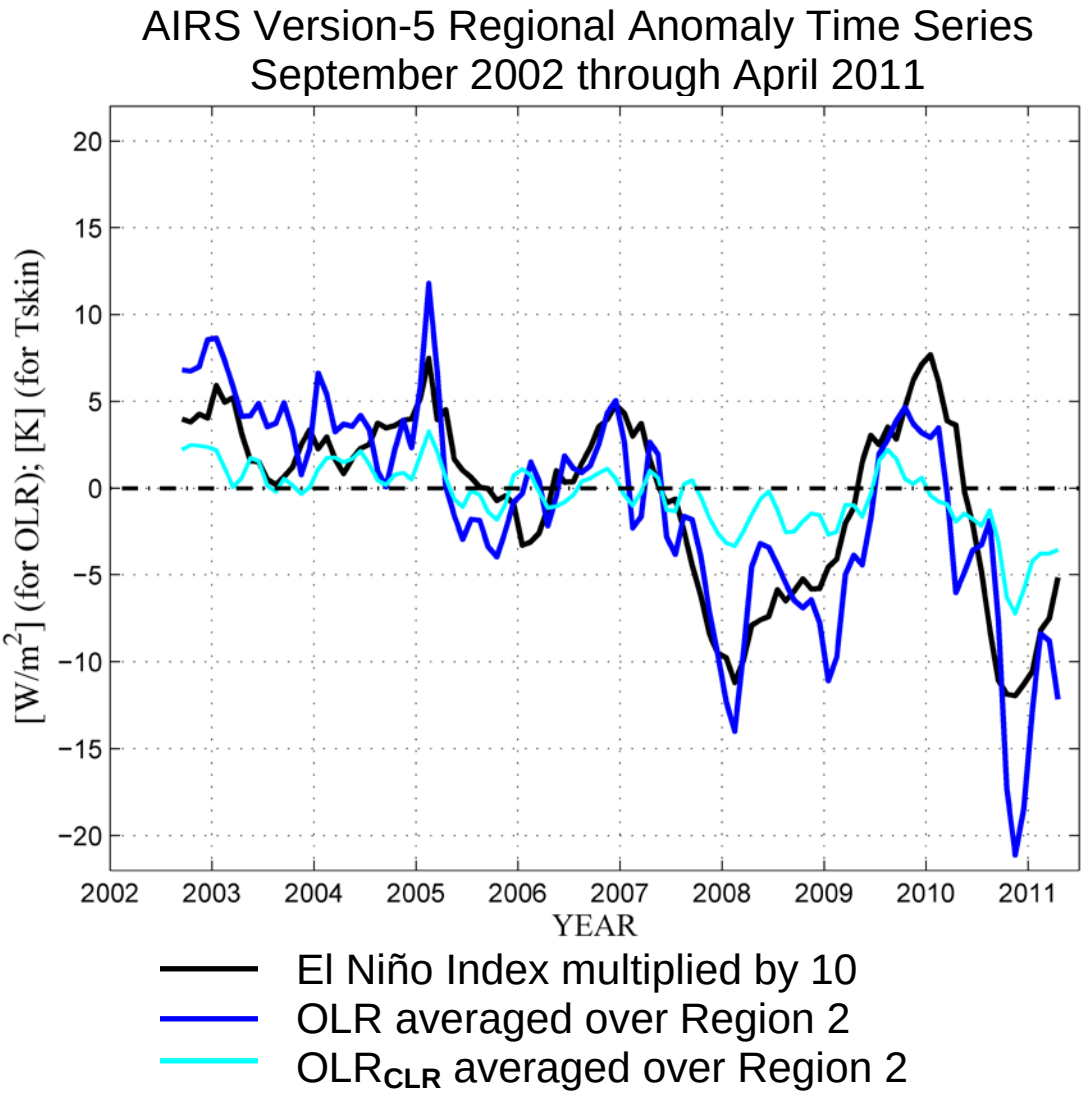

Figure 13b. AIRS OLR and OLR_{CLR} anomaly time series averaged over OLR Region 2 superimposed on the AIRS El Niño index multiplied by 10 without a time lag.